3536

NACA TN 2110

TECH LIBRARY KAFB, NM
0065416

NATIONAL ADVISORY COMMITTEE FOR AERONAUTICS

TECHNICAL NOTE 2110

INTERFEROMETER CORRECTIONS AND MEASUREMENTS OF LAMINAR BOUNDARY LAYERS IN SUPERSONIC STREAM

By Robert E. Blue

Lewis Flight Propulsion Laboratory
Cleveland, Ohio

Washington
June 1950

AFMDC
TECH
AUG 2011

319.98/41

TECH LIBRARY KAFB, NM

0065416

NATIONAL ADVISORY COMMITTEE FOR AERONAUTICS

TECHNICAL NOTE 2110

INTERFEROMETER CORRECTIONS AND MEASUREMENTS OF LAMINAR BOUNDARY LAYERS IN SUPERSONIC STREAM

By Robert E. Blue

SUMMARY

The laminar boundary layer on a flat plate in a supersonic stream was investigated by means of a Zehnder-Mach interferometer and a total-pressure probe. The density gradient in the boundary layer on the plate necessitated consideration of the effect of light refraction on the interference data.

Density and velocity distributions, which were obtained with the two instruments for a range of local Reynolds number from 0.318×10^6 to 1.08×10^6 at a nominal Mach number of 2.02, compared favorably with laminar-boundary-layer theory. Skin-friction coefficients calculated from the boundary-layer profiles were larger than predicted by theory.

INTRODUCTION

Increasing application of light-interference methods to aerodynamic and thermodynamic studies has indicated that the procedure of obtaining and evaluating interference photographs differs considerably, depending on the study to which the method is applied. Factors such as light refraction, definition of a solid surface, and nonuniformities in the density field may be of little or no concern in one application, for example, when measuring pressure distributions on an airfoil in subsonic flow (reference 1); whereas they may cause an appreciable error for another application, such as the measurement of temperature distribution around a heated body (reference 2). Even when interferometry is applied to the specific problem of obtaining density distributions in a boundary layer of air near a solid surface, these factors can cause errors of varying degrees depending on the type of density profile (laminar or turbulent), the boundary-layer thickness, and the total density change across the boundary layer.

Boundary-layer investigations on an airfoil and a flat plate in subsonic flow were made at the Hermann Göring Institute by Zobel in 1940 (reference 3). The boundary layers were relatively thick (of the order of 0.1 in.) and of a turbulent nature, with a total density change across the layer of approximately 2.8 percent of the density at the edge of the boundary layer. Errors in the method apparently were assumed to be negligible, inasmuch as no discussion was devoted to them.

A boundary-layer investigation, conducted at the NACA Lewis laboratory and presented herein, is similar to the earlier work done in Germany, except that errors caused by light refraction and an inability to distinguish the exact location of the surface are amplified because the boundary layer studied is much thinner (0.030 in.), the density change larger (42 percent), and the profile of a laminar type. A laminar boundary layer concentrates most of the total density change across the layer in a relatively narrow region, whereas for a turbulent profile the density change is more evenly distributed. The high density gradients that exist in a laminar layer amplify errors caused by light refraction.

Although some information was obtained regarding the behavior of a laminar boundary layer on a flat plate in a supersonic stream both by interferometer and pressure-probe measurements, the experiments and the analysis were made with the intention of systematically organizing the steps required to evaluate and to correct interference data and to estimate the error in the final result. With this information, a more detailed study of heat-transfer and boundary-layer phenomena can be undertaken using the interferometer as the primary measuring instrument.

APPARATUS AND PROCEDURE

Interferometer

A Zehnder-Mach type interferometer was used for this investigation. The construction and the operation is conventional and will not be discussed in detail as there are many excellent descriptions of the problems of design, construction, and operation of this type of instrument. (For example, see references 4 and 5.)

A sketch of the interferometer and wind-tunnel installation is shown in figure 1. The collimator consists of an f/1.3, 1/2-inch focal-length lens focusing the light from a high-pressure mercury-vapor light on a 0.008- by 0.125-inch slit located at the principal

focus of an f/2.5, 12.5-inch focal-length lens. The camera lens is an f/7.5 lens with an 18.5-inch focal length. The light is filtered for the mercury green line 5461 A.

Supersonic Wind Tunnel and Model

The measurements were made on the boundary layer developed on a flat steel plate 4 inches long and 3.6 inches wide. The plate had a 12° wedge angle on the bottom. The leading edge was honed to give the sharpest edge possible. The angle of attack could be varied between ±3°. The plate completely spanned the 3.6-inch square test section of a two-dimensional supersonic tunnel designed by the method of characteristics for a Mach number of 2.08. Flow observation was through 1/2-inch, optically flat windows set in aluminum side plates. The wind tunnel and flat plate with one side plate removed is shown in figure 2. Provisions were made for inserting a total-pressure tube, which is shown above the plate in figure 2, to probe the boundary layer. Distance from the surface to the bottom of the probe tip was measured with a micrometer and is considered accurate to less than 0.0005 inch. Contact of the probe with the surface was indicated by an oscilloscope, which also provided a method of detecting probe oscillation. The oscilloscope was wired in series with a battery; one end of the circuit was connected to the plate and the other end to the probe. A flip in the oscilloscope trace occurred when the plate and the probe, which were electrically insulated from each other, came into contact. The pressure measured by the probe was assumed to be the pressure at the geometric center of the probe opening. The over-all height of the probe tip was 0.0026 inch. The shape of a typical probe opening is shown in figure 3. Twelve static-pressure taps and three thermocouples in the surface provided a method of determining the nature of the pressure gradient and the temperature along the plate.

Air Supply

The air supplied to the tunnel had a dew point of 410° R or lower. Inlet pressure and temperature could be varied over the ranges of 11 to 40 inches of mercury absolute and 540° to 590° R, respectively, which gave a stream Reynolds number range of 1.04×10^5 to 4.27×10^5 per inch in the test section.

Preliminary Adjustments

Before any boundary-layer data were taken, a preliminary experiment was made in which the angle of attack of the plate was varied over the range of $\pm 3^{\circ}$ in order that a zero pressure gradient would exist over the length of the plate. The change in pressure distribution was negligible over this range of angle of attack. A second criterion for adjustment therefore was that the shock wave from the leading edge of the plate have a minimum strength. The interferometer was used to observe the wave while the angle of attack was continuously changed over the entire range of possible angles. The plate was then set to the angle where the disturbance appeared to be the weakest. This adjustment was made when the tunnel was operating with inlet air at a pressure of 40-pound gage rather than 5-pound-gage used when measurements were made. The purpose of the higher pressure was to amplify the density difference and the changes in the density difference across the shock wave. Dry 40-pound air was generally unavailable for quantitative measurements. An illustrative interferogram of the leading-edge shock wave is shown in figure 4. The strength of the disturbance on the upper side of the plate (the side on which the boundary layer was investigated) can be compared with the compression region resulting from the turning on the underside of the plate. Pressure distributions (fig. 5) were recorded at various inlet pressures for the final orientation of the plate.

During the experimental portion of this investigation, it was noted that extreme care must be taken to prevent regions of local turbulence from developing at the surface of the plate. Such regions can be caused by leaky static-pressure orifices or by specks of dirt on the surface that are so small as to be almost invisible.

ANALYSIS

Total-Pressure Data

The conventional assumption that the static pressure is constant through the boundary layer along a line normal to the surface was used in calculating the Mach number distribution from the ratio of measured total pressure to wall static pressure by means of the Rayleigh equation for Mach numbers greater than 1 and by the isentropic-flow equation for Mach numbers less than 1. Mach number, ambient temperature, and total temperature are related at any point in the flow by the one-dimensional energy equation, from which the following expression is derived:

$$\frac{t}{t_1} = \frac{T}{T_1}\left(\frac{1 + 0.2\ M_1^2}{1 + 0.2\ M^2}\right) \tag{1}$$

(All symbols used in this report are defined in appendix A.) The ratio of specific heats was taken as 1.4. In order to calculate ambient-temperature distribution from the measured Mach number using equation (1), the distribution of the total temperature must be known. Laminar-boundary-layer theory has shown that only for the case of a Prandtl number Pr equal to 1 can the assumption be made of constant total temperature through the boundary layer. It is known, however, that $Pr \approx 0.72$ for air. Inasmuch as no means were available to measure the total-temperature distribution, the theory developed in reference 6 was used to calculate the total temperature as a function of the dimensionless distance variable $y\sqrt{\frac{u_1}{\nu_1 x}}$ for a Mach number M_1 measured at the edge of the boundary layer by the total-pressure probe. A typical total-temperature distribution is plotted in figure 6. Values of total-temperature ratio taken from the theoretical curve and measured values of Mach number were substituted in equation (1) to obtain t/t_1. The density ratio ρ/ρ_1 is given by

$$\frac{\rho}{\rho_1} = \frac{t_1}{t} \tag{2}$$

because p is assumed constant. The velocity ratio u/u_1 was calculated from

$$\frac{u}{u_1} = \frac{t}{t_1}\sqrt{\frac{M}{M_1}} \tag{3}$$

Interference Data

The method used to analyze an interferogram is determined by the basic adjustment of the instrument. Adjustment to give interference fringes parallel to the line along which the density distribution is to be measured, in this case perpendicular to the plate surface, produces a photograph that requires the least work to analyze. A vertical-fringe adjustment was used in this case, inasmuch as the flat plate was horizontal. The indicated boundary-layer profile was calculated by a method described in reference 2.

The principle of the method of analysis is illustrated in figure 7. If the density were constant throughout the field, the center line of fringe A in the figure would pass through point P and would be everywhere parallel to the dotted line that is perpendicular to the surface. The shift of one fringe at P indicates that there is one less wavelength (less because the density decreases) in the path of the light appearing to come from P than there would be if the density at P were the same as at Q. The difference in density $\Delta\rho$ between the points P and Q in terms of the fringe shift N (reference 2) is

$$\Delta\rho = \frac{\lambda_0}{kL} N \tag{4}$$

For boundary-layer studies, the density at the point P is associated with the distance of the point from the surface. This distance was measured directly from the interferogram negative by means of a comparator and was converted to actual distance from the surface by dividing by the magnification of the photograph.

In order to calculate the ratio of boundary-layer density to density at the edge of the layer, the absolute density at the edge of the layer must be known. This density can be calculated either from pressure and temperature measurements or from a measure of the number of monochromatic fringes that traverse the position where the density profile is to be evaluated when the tunnel changes from a no-flow to a flow condition. The method using the monochromatic fringes is inaccurate when the boundary layer on the tunnel windows occupies an appreciable portion of the tunnel span. The stream density was therefore calculated from the wall static pressure and the calculated free-stream ambient temperature. The density profile obtained in the manner just described is hereinafter referred to as the "indicated" density profile, as distinguished from the actual density profile.

Errors in Interference Data

The indicated density profile may or may not be an accurate representation of the profile existing in the boundary layer on the plate. In order to determine the degree of approximation to the actual density distribution, an analysis was made of the factors affecting the formation of boundary-layer interference fringes when the density profile has a zero density gradient at the surface and at the edge of the boundary layer and rises monotonically to a maximum value between the zero values. This analysis is perhaps

more valid for a laminar profile than for a turbulent profile. The analysis indicates the necessary steps required to correct interferometer data and also gives an estimate of the error in the final results. The errors have been divided into three general catagories: those caused by (a) light refraction, (b) interferogram evaluation, and (c) tunnel-window boundary layer.

Refraction errors. - The principal cause of errors in the interference data is the refraction of the light in the nonuniform density field of the boundary layer. When the density at the surface is less than in the stream, the light is bent away from the surface, as schematically shown in figure 8. The path of a light ray through the boundary layer can be calculated in terms of the coordinates z and y from the law of refraction for non-homogeneous media, which was obtained from Fermat's principle. If density variations are assumed to exist only in the plane of the light path, this law can be expressed by

$$\frac{y''}{1 + y'^2} = \frac{1}{n}\frac{\partial n}{\partial y} - \frac{1}{n}\frac{\partial n}{\partial z} y' \tag{5}$$

where the refractive index of air n is related to air density by the experimentally determined law of Biot and Mascart

$$\frac{n - 1}{\rho} = k = 0.1166 \text{ (cu ft/slug)} \tag{6}$$

when

$$\lambda_0 = 5461 \text{ A}$$

If light were not refracted but passed through a two-dimensional boundary layer parallel to the surface, and if all other errors were negligible, the interferometer would indicate a density profile identical to the actual profile. Refraction, however, causes the following errors:

1. Averaging errors. Instead of traversing the boundary layer at a constant density, the light passes through layers of increasing density. The average density along the light path is therefore higher than the density at the entrance height. The difference between the local-stream and average densities is therefore less than the difference between the local-stream and entrance densities. Because the density difference is directly proportional to fringe shift (equation (4)), the fringe shift is less than would exist with no refraction.

2. Window errors. The light, after passing through the boundary layer, makes an angle θ_e with the plate surface at the inside of the tunnel window. On striking the glass at an angle, the light is refracted according to Snell's law ($\sin \theta_e = n_g/n_{air} \sin \theta_r$), and passes through the glass in a straight line at an angle θ_r with the surface. At the outside surface of the window, the light is again refracted back to the original angle θ_e. Without refraction in the boundary layer, the light would travel a distance τ (the glass thickness) through the glass, or an optical-path length of $n_g\tau$. With refraction, the optical path becomes $n_g\tau/\cos \theta_r$, which is an increase in optical path over the undeviated path by the amount $n_g\tau(1 - \cos \theta_r)/\cos \theta_r$. This quantity, divided by the wavelength of the light in a vacuum, is the decrease in fringe shift between a ray through the boundary layer and a ray through the stream. The density indicated by the interferometer will therefore be higher than it would be if the effect were not present. (The boundary layer and the glass window have an opposite effect on optical-path length.)

3. Displacement errors. As a general rule, the light will not appear to come from the point in the object plane at the distance from the surface at which the light entered the tunnel. Instead it will appear to originate at the point y_a (fig. 8) where the backward extension of the light ray from the outside of the tunnel window intersects the object plane of the camera lens. The location of this point is influenced by: (a) the emergent height of the light y_e, (b) the emergent angle θ_e, (c) the thickness of the tunnel window τ, and (d) the location of the object plane.

The indicated density is therefore an average density along a curved light path and is increased in value by the additional path through the tunnel window, and appears to originate at a somewhat arbitrary height above the surface, determined by the refraction of the light in the boundary layer and the geometry of the optical system.

An estimate of the approximate magnitude and relative importance of each of these errors was made by using equation (5) to determine the light path through a boundary layer having a density distribution corresponding to a cosine curve. The assumed cosine profile resembles a laminar density profile in that it has the previously mentioned characteristic of zero density gradient at the plate surface and at the edge of the boundary layer. The density at the edge of the layer, the ratio of stream density to wall density, and the

boundary-layer thickness were chosen from experimentally measured values at an inlet pressure of 30 inches of mercury absolute and a total temperature of 560° R. A comparison of the assumed cosine density profile and the faired curve of the profile calculated from the total-pressure measurements made at these conditions is shown in figure 9. The light path and error calculations for the assumed profile are shown in appendix B. From calculated light paths, the averaging, window, and displacement errors were each evaluated for a number of incident heights of light rays in order to obtain enough points to plot a distribution curve for each error. The sum of the three errors is the total error due to refraction. The four error distribution curves are plotted in figure 10. These results show that an uncorrected boundary-layer profile indicated by an interferometer for conditions such as the assumed ones is of little value in calculating aerodynamic data. By extending the calculations to other conditions of inlet pressure and temperature but still assuming the cosine density profile, the maximum total refraction error was found to be less than 1 percent in a tunnel span of 3.6 inches if the ratio $\sqrt{\rho_1 - \rho_w}/\delta$ is less than 0.19.

Correction of refraction errors. - Analysis of boundary-layer-interference data is the reverse problem of the one previously considered; that is, given an indicated density profile, find the density distribution through which the light passed. Unfortunately, the indicated profile provides insufficient information with which to make the necessary calculations. Any process of correction will therefore require certain assumptions and must be developed with the idea of producing a reasonably accurate result with a minimum of work.

A possible method of correction that was considered makes use of the assumption that the indicated profile is a first approximation to the correct profile. Light paths calculated from a numerical integration of the refraction equation could be used to obtain values for the various errors that, when applied to the indicated profile, would give a corrected curve for the boundary-layer density distribution. Such a process would be of doubtful accuracy if the indicated profile was very different (5-percent maximum error in density) from the actual profile because of the sensitivity of the light path to values of the density gradient. For example, in figure 11, where the slope of the assumed and indicated profiles differ, the method is probably invalid. Also, the calculations would be lengthy unless programed for an automatic calculator.

For the case where time is not a factor in obtaining the interference photographs, the following method, which was applied to the data presented, can be used: Two interference photographs were taken at each condition, one with the camera focused on the center of the tunnel and the other with the camera focused on the edge of the plate nearest the light source. The indicated profiles calculated from the two photographs differed only in that the apparent height above the surface at which each light ray appears to originate is shifted. The emergent angle θ_e of the light leaving the tunnel can be found at a given value of the density ratio by taking the difference in the apparent heights indicated for that density ratio by the two profiles and then dividing the difference by the distance between the object planes for the two photographs. The angle θ_e is related to the density difference between the incident and emergent points on the light path by the equation

$$\theta_e = \sqrt{2k\rho_1 \left[\left(\frac{\rho}{\rho_1}\right)_e - \left(\frac{\rho}{\rho_1}\right)_i\right]} \tag{7}$$

which was obtained by integrating equation (5), neglecting a variation of the index of refraction in the z-direction (two-dimensional boundary layer). The two approximations made in deriving equation (7) are that $\tan \theta_e = \theta_e$ and that $n_e^2 - n_i^2 = 2n_i(n_e - n_i)$. If the density is assumed to change linearly in the y-direction between the incident and emergent points on the light path, the following relations that were found from the refraction equation for a constant density gradient (appendix C) can be applied:

$$\left(\frac{\rho}{\rho_1}\right)_{av} - \left(\frac{\rho}{\rho_1}\right)_i = \frac{k\rho_1 L^2}{6}\left[\frac{\left(\frac{\rho}{\rho_1}\right)_e - \left(\frac{\rho}{\rho_1}\right)_i}{y_e - y_i}\right]^2 \tag{8}$$

$$(y_e - y_i)^2 = \frac{1}{2}\, k\rho_1 L^2 \left[\left(\frac{\rho}{\rho_1}\right)_e - \left(\frac{\rho}{\rho_1}\right)_i\right] \tag{9}$$

Substituting equations (7) and (9) in (8) yields

$$\left(\frac{\rho}{\rho_1}\right)_{av} - \left(\frac{\rho}{\rho_1}\right)_i = \frac{\theta_e^{\,2}}{6\rho_1 k} \tag{10}$$

which is an expression for the averaging error. The window error can be found in terms of the fringe shift N_g from equation (4).

$$\left(\frac{\rho}{\rho_1}\right)_{ind} - \left(\frac{\rho}{\rho_1}\right)_{av} = \frac{\lambda_0}{\rho_1 kL} N_g \tag{11}$$

A plot of the fringe shift N_g against the angle θ_e of the light when it strikes the window for a 1/2-inch thickness of crown glass ($n_g = 1.52$) is shown in figure 12. The values of the two errors, when subtracted from the indicated density, give a number approximately equal to the density ratio at the height y_i. Equations (A8) (appendix A), (7), and (9) lead to an expression for y_i in terms of the apparent height and emergent angle, both of which are known from the photographic data:

$$y_i = y_a + \theta_e \tau \left(\frac{n_g - 1}{n_g}\right) + \left(FL - \frac{L}{2}\right)\theta_e \tag{12}$$

The fraction F, determined by the location of the object plane (fig. 8), is 1/2 when y_a is read from the curve corresponding to the center-focus interferogram. The resulting equation is obviously approximate because it only allows y_i to be greater than or equal to y_a, whereas the plot of $\left(\frac{\rho}{\rho_1}\right)_i - \left(\frac{\rho}{\rho_1}\right)$ in figure 10 shows that y_i can be less than y_a. The approximation results because of the constant-density-gradient assumption.

In order to determine the reliability of the assumptions involved in the derivation of the correction process, the process was applied to the indicated profiles calculated in appendix B. The agreement between the corrected points and the original assumed cosine density profile is a measure of the accuracy of the process. The corrected data points are shown in figure 13 with the assumed density profile and the indicated density profiles for the two locations of the object plane.

The faired curve for the indicated profile with the camera focused on the edge of the plate (fig. 13) has been shifted to the left by 0.0023 inch from the curve shown in figure 11. The reason can be explained with the aid of figure 8. The intersection of the dashed line, which represents the backward extension of an emergent light ray, changes from the height y_a at the center to a point

below the surface when the object plane is shifted to the edge of the plate. Some of the light passing through the boundary layer therefore appears to come from a point below the surface of the plate. The distance below the surface depends on the emergent angle and the height of the ray. The calculations for the indicated density profile in figure 11 showed that the lowest point from which the light would appear to originate would be 0.0023 inch below the shadow cast by the surface of the plate. In the evaluation of a photograph, the lowest point is considered as the surface, thereby introducing a displacement of the indicated profile equal to the shift of the surface. Because the y values used to calculate the emergent angle of the light are both referred to the same axis, the measured profile at the edge of the plate must be shifted to refer to the axis used in the evaluation of the indicated profile at the center of the tunnel. An interferogram showing the shift of the surface is shown in figure 14(a). The effect is markedly pronounced because a double exposure was made: one without flow, showing the actual location of the surface; and one with flow where the surface appears in the position to which it was shifted. With a laminar velocity profile, a double exposure is not required in order to detect the shift of the surface. Because of the zero density gradient at the surface of the plate, the light that just grazes the surface will not be deviated in passing through the tunnel. This light will therefore arrive at the same place on the negative both with and without flow. It shows up as a bright line or a discontinuity in the boundary-layer interference fringes. The discontinuity and the brightness just above the surface can be seen in figure 14(b).

The corrected data points in figure 13 furnish insufficient information to plot a complete density profile. As a result of shifting the indicated profile in the aforementioned manner, values of the emergent angle of the light can only be found for the upper part of the boundary layer. Data with which to calculate the emergent angle in the region near the surface could be obtained by taking and evaluating a third photograph with the camera focused on the edge of the plate nearest the camera. Such a photograph could not be obtained in this investigation because of physical limitations of the equipment used. The behavior of the corrected density profile was therefore estimated in the region where data were unavailable.

The results of an application of the correction process to an experimentally determined indicated density profile are shown in figure 15, along with the indicated profiles for the camera focused on the center and edge of the plate. The inlet conditions under which

these data were obtained were a free-stream total pressure of 29.33 inches of mercury absolute and a free-stream total temperature of 560° R, which are very close to the conditions corresponding to the assumed profile.

High-speed and normal-speed interference motion pictures were taken of the boundary layer in order to detect any fluctuations in the density profile, either instantaneously or over an extended period of time. The interference fringes of the boundary layer were steady in both cases for inlet pressures above 12.5 inches of mercury absolute. Below this pressure, the boundary layer separated from the surface and fluctuated up and down. This separation was caused by the starting shock, which had moved to the rear edge of the plate. Interference data have been evaluated only over the range where the boundary layer did not change with time. The process of taking two photographs at each condition over a finite interval of time in order to evaluate and to correct the interference data therefore did not cause any inaccuracies. A method has been suggested of adapting the correction process to the study of transient phenomena by using an infinite fringe adjustment of the interferometer and taking simultaneous interferograms of two object planes.

The calculations of the refraction errors and the correction process that is applied to the indicated density profile both make use of the assumption that light enters the boundary layer parallel to the surface. In actual practice, all the light cannot be parallel because the light source must have a finite extension. For the collimating system used in this investigation, the maximum angle between any light ray and the central ray, which was adjusted parallel to the surface, was 0.00032 radian. In order to show that the light path through the boundary layer can be considered independent of the incident angle of the light, for small angles, the refraction equation was integrated for an arbitrary density distribution. Differentiation of the resulting equation

$$z = \int \frac{dy}{\sqrt{\left(1 + \theta_i^2\right) \frac{n^2(y)}{n_i^2} - 1}} \tag{13}$$

with respect to θ_i shows that the percentage change of z with θ_i is of the same order of magnitude as θ_i. The assumption of parallel light is therefore justified.

Interferogram-evaluation errors. - Inaccuracies in measurements from an interferogram do not arise in the measuring instrument. They are dependent on the judgment of the operator in choosing the exact location of a particular point on the negative. The following effects add to this problem:

1. In the region near the edge of the boundary layer, where the density gradient is relatively small, the diffuseness of the interference fringes causes difficulty in locating points corresponding to fractional fringe shifts. The measurements in this region are therefore the least accurate of any of the distance measurements.

2. The surface of the plate is not sharply defined in an interferogram because of the angular deviation of the light from the extended source. A combination of reflected and defracted light from the plate interferes with the light from the beam that travels around the tunnel and the interference produces the pattern at the surface seen in figure 16. This region extends for a distance of 0.0054 inch above the surface and causes an equivalent uncertainty in the location of the surface. In order to facilitate a more accurate estimate of the location of the surface, a photograph was taken of a known-size wire lying on the plate. By using the magnification of the picture and the wire size, the distance from the top of the image of the wire to the position at which the image of the surface should have been located was measured on the negative. Inasmuch as the appearance of the negative at this point was known, an estimate of the location of a similar point was made for each boundary-layer interferogram. The error is therefore much less than 0.0054 inch; the value depends on the judgment of the evaluator.

3. Developing time for the interferograms should be so chosen that the bright and dark fringes are of equal width because measurement of fractional fringe shifts in evaluating the pictures is desirable. Overdeveloping shifts the boundary line between a bright and a dark fringe and widens the bright fringe, as shown in the interferogram of figure 17. The location of the center of a fringe is unaffected by overdeveloping.

4. Inasmuch as the interference measurements were made directly on the negative of the interferogram, no errors due to distortions in enlarging resulted. Distortions due to the optical system or to film shrinkage, however, are possible. By photographing a grid of uniform size and then measuring the distortion of the grid, the magnitudes of such errors were found to be negligible. The magnification of the photographs was also found from the photograph of the grid.

Tunnel-window boundary-layer errors. - The indicated density, calculated from equation (4) for a fringe shift N measured from an interferogram, has been assumed to represent the sum of two terms according to the equation

$$\rho_{ind} = \rho_{av} + \frac{\lambda_0}{kL} N_g \tag{14}$$

Because of the boundary layer on the tunnel windows, the assumption of a two-dimensional boundary layer on the plate used in arriving at equation (14) is not fulfilled. Equation (4) therefore yields a density

$$\rho'_{ind} = \rho_1 - \frac{\lambda_0}{kL} N \tag{15}$$

which differs from ρ_{ind}. An expression for this difference can be obtained by considering two rays of light, one traversing the free stream above the plate and the other passing through the boundary layer. If the same boundary layer on the windows is assumed for each light path, the average density traversed by each ray is

$$\left.\begin{aligned} &\text{for free stream,} \\ &\rho_f = \frac{\rho_1(L - 2\delta_g) + 2\int_0^{\delta_g} \rho(z)dz}{L} \\ &\text{for boundary layer,} \\ &\rho_b = \frac{\rho_{av}(L - 2\delta_g) + 2\int_0^{\delta_g} \rho(z)dz}{L} + \frac{\lambda_0}{kL} N_g \end{aligned}\right\} \tag{16}$$

The fringe shift N used in equation (15) corresponds to the density difference $\rho_f - \rho_b$. Replacement of the last term of equation (15) with the expression for $\rho_f - \rho_b$ given by equation (16) yields

$$\rho'_{ind} = \left(\rho_{av} + \frac{\lambda_0}{kL} N_g\right) + (\rho_1 - \rho_{av}) \frac{2\delta_g}{L} \tag{17}$$

Comparison of equations (14) and (17) shows that the density ρ'_{ind} used in the calculations is larger than ρ_{ind} by the amount of the last term in equation (17), which introduces an equivalent error. Written in terms of density ratio, the error is

$$\left(\frac{\rho}{\rho_1}\right)'_{ind} - \left(\frac{\rho}{\rho_1}\right)_{ind} = \left[1 - \left(\frac{\rho}{\rho_1}\right)_{av}\right] \frac{2\delta_g}{L} \tag{18}$$

Errors caused by end effects will therefore vary inversely with the span of the tunnel. The largest error will be for the ray traveling closest to the surface. For example, if the ratio of wall to stream density is 0.584 and the boundary layer on the tunnel window is 1/10 inch thick, the largest error for a tunnel 3.6 inches wide will be 4.0 percent. The error in this calculation due to the assumption that the boundary layer on the windows is the same at all points will be a second-order effect.

The tunnel width to be used for a particular boundary-layer investigation should be such as to make the sum of the refraction and the end-effect errors a minimum. Equation (8), which gives an order-of-magnitude estimate of the largest refraction error as being directly proportional to the square of the tunnel span, can be used to find the optimum width that balances the two errors when combined with equation (18). Calculations show that the tunnel width for this investigation should have been approximately 1.5 inches. Aerodynamic considerations may modify this calculation.

Two-dimensional boundary layer. - Interferometer data will still be in error when corrected by the preceding methods if the boundary-layer flow is not two-dimensional. In order to determine how closely this condition of two-dimensionality was met in these experiments, total-pressure surveys were made of the boundary layer at three spanwise positions on the plate. Density profiles calculated from these surveys using equation (1), but assuming constant total temperature, are plotted in figure 18. The surveys were made at three Reynolds numbers. The agreement between the three curves at each condition is an indication of the two-dimensionality of the boundary layer. Profiles for the lowest Reynolds number (fig. 18(a)) agree most closely. These profiles are probably an inaccurate representation of the actual density distribution because of the assumption of constant total temperature.

Velocity-profile calculations. - Velocity profiles were calculated from the interference data by assuming a theoretical total-temperature distribution, as was done for the total-pressure data. The calculation differs slightly in one respect. An accurate value of density at the wall could not be obtained from an interferogram. The wall density was therefore taken to be the value corresponding to the measured surface temperature. According to the energy equation, however, surface temperature is determined by the local stream Mach number M_1 and the temperature recovery factor η_t by the equation

$$\frac{T_w}{T_1} = \frac{1 + 0.2\ \eta_t M_1^2}{1 + 0.2\ M_1^2} \tag{19}$$

A value of η_t of 0.845 for a Prandtl number Pr of 0.72 is found in reference 6. Inasmuch as the measured value of surface temperature indicated a Prandtl number higher than 0.72, the wall temperature calculated from the measured M_1 with equation (19), using $\eta_t = 0.845$, was lower than the measured surface temperature. From equations (1) and (3), the condition for zero velocity at the wall is

$$\frac{T_w}{T_1}\frac{\rho_w}{\rho_1}\left(1 + 0.2\ M_1^2\right) = 1 \tag{20}$$

In order to use the curves given in reference 6 and at the same time satisfy equation (20) for the measured values of ρ_w/ρ_1 and M_1, it was therefore necessary to adjust the value of M_1 used in equation (19). The new value of M_1 was used to calculate the total-temperature distribution from the theory. This value was approximately 0.05 larger than the measured M_1. The measured values of ρ/ρ_1 and M_1 and the calculated total-temperature distribution furnish the necessary quantities to calculate Mach number distribution. The velocity ratio was calculated from the density and the Mach number curves using equations (2) and (3).

RESULTS AND DISCUSSION

Velocity and Density Profiles

The data needed to calculate velocity and density profiles were obtained by interferometer and pressure-probe measurements in the

local Reynolds number range Re_x of 0.318×10^6 to 1.08×10^6. Mach number changed slightly over this range of operating conditions; the nominal value was 2.02. The interference photographs taken with the camera focused on the center of the tunnel are shown in figure 19. Indicated density profiles measured from these photographs at a position $2\frac{1}{2}$ inches from the leading edge of the plate and the corresponding corrected profiles are plotted in figures 20(a) and 20(b), respectively. The theoretically more interesting plot of the ratio of density in the boundary layer to density at the edge of the boundary layer against the dimensionless distance variable $y\sqrt{\frac{u_1}{\nu_1 x}}$ is shown in figure 21(a) for the interference data and in figure 21(b) for the total-pressure data. These figures include a curve calculated from the theory presented in reference 6 for the case of an unheated, uncooled plate in a supersonic stream of Mach number 2. Similar experimental and theoretical curves for the velocity profiles are shown in figures 22(a) and 22(b).

The density profiles calculated from the total-pressure data are nearly the same in shape as the theoretically calculated curve. The shifting of the experimental profiles to the right of the theoretical curve might be due to a random error in the experiments because no apparent relation exists between the shift of the profiles and the variables pressure, temperature, or Reynolds number.

Relatively good agreement exists between theory and the profiles obtained from pressure measurements. The interferometer density profiles are below the pressure measurements and theory near the edge of the boundary layer. The lower density indicated for this region may be connected with the fact that the interferometer measures the thermal boundary layer, whereas the total-pressure probe measures the velocity layer. The increasing inaccuracy of the indicated profiles and of the correction process at the higher inlet pressures, however, is more probably the explanation of the discrepancy. A comparison of figures 22(a) and 22(b) shows that the profile for the lowest inlet pressure is in close agreement with the total-pressure profile. The agreement of the other curves decreases as the inlet pressure increases. Application of the correction process to the indicated profile calculated for the assumed density variation produced a corrected curve having a maximum error of 1.2 percent. All the factors that influence the indicated density profile in actual practice have probably not been accounted for, inasmuch as the errors in the profiles of figure 21(a) are apparently

greater than this small percentage. For example, the effect of boundary layer on the tunnel windows is disregarded in both the evaluation and the correction of the indicated profile.

The boundary-layer thickness taken from the interference data is considerably greater than that indicated by the pressure data. The reason is apparent when the boundary layer in the corners between the plate and the windows is considered, as in reference 7. The boundary layer on the plate and on the window must form a continuous variation of the density around the corner rather than the abrupt right-angle change that would exist if the two boundary layers did not interact with each other. This interaction has the effect of thickening the boundary layer on the plate near the corners. A ray of light that enters the tunnel at a point just at the edge of the boundary layer will therefore travel a shorter optical path than a ray passing through at a height high enough to be unaffected by the corner boundary layer because of the reduced density in the corner regions that extends above the edge of the boundary layer. Interference measurements are therefore useful only for an approximate estimate of the boundary-layer thickness.

Boundary-layer thickness taken from the density profiles of the pressure measurements is plotted in figure 23 with a curve calculated from the theory of reference 6. The theoretical curve gives values approximately 30 percent lower than the measured values. The experimental points, however, are insufficient to establish a trend.

Skin Friction

The velocity and density profiles were used to calculate the section skin-friction coefficient C_f to a position $2\frac{1}{2}$ inches from the leading edge of the plate by a graphical integration of the Kármán momentum equation, which was used in the following form:

$$C_f = \frac{D_f}{\frac{1}{2}\rho_1 u_1^2 xL} = \frac{2}{x}\int_0^{\delta} \frac{\rho}{\rho_1}\frac{u}{u_1}\left(1 - \frac{u}{u_1}\right)dy \qquad (21)$$

Values of C_f are plotted in figure 24 as a function of local stream Reynolds number. These points are compared with curves from the incompressible and compressible laminar-boundary-layer theory. The results indicate that the laminar skin-friction coefficient increases

with Mach number, rather than decreasing as predicted by theory. The experimental conditions are inconsistent with the assumptions of the theory in that a disturbance produces rotational flow at the leading edge. This rotational flow may be equivalent to starting with an initial boundary layer at the leading edge. If such is true, the value of x used to calculate Re_x and C_f should be larger than the actual distance ($2\frac{1}{2}$ in.) by an amount that would be required to develop the initial boundary layer without the leading-edge shock. As an illustration, the point $Re_x = 0.61 \times 10^6$, $C_f = 0.00205$ (fig. 24) has been recalculated for $x = 3\frac{1}{2}$ inches. The new values are $Re_x = 0.72 \times 10^6$ and $C_f = 0.00147$, which is a point slightly below the compressible-theory curve. The measured values of C_f agree with the theory in that they decrease with an increase in $\sqrt{Re_x}$. The agreement between the values of the skin-friction coefficient calculated from the total-pressure and interferometer measurements, if used as a measure of accuracy of the interference method, shows that the correction process overcorrects when light refraction is small (low Reynolds number, fig. 24) and undercorrects when the refraction is large. The interference measurements give a value that is 9 percent below the total-pressure measurements at the lowest Reynolds number and 5 percent above at the highest Reynolds number.

Recovery Factor

The recovery factor η_t, which is the fraction of the kinetic energy of the undisturbed flow that raises the effective temperature of the plate to a value above the ambient temperature, was calculated from the relation

$$\eta_t = \frac{t_w - t_1}{T_0 - t_1} \tag{22}$$

which was obtained from the definition of total temperature and the equation defining η_t. The temperatures t_w and T_0 were measured and t_1 was computed from M_1 and T_0. Although the recovery factor is theoretically dependent only on the Prandtl number of the air, the results of these measurements showed a tendency for η_t to increase with Reynolds number. The experimentally determined values are plotted in figure 25 as a function of the Reynolds number in the test

section. An integration of the energy equation for incompressible laminar flat-plate flow, performed by Pohlhausen (reference 8), predicts a recovery factor of 0.849, which is the square root of the Prandtl number of 0.72. (Reference 6 gives 0.845 for Prandtl number of 0.72.) The measured values are slightly larger than 0.87 but not as large as 0.90, which has been found for turbulent flow. A recovery factor of 0.87 corresponds to a Prandtl number of 0.76.

CONCLUSIONS

Errors due to light refraction must be considered in any boundary-layer investigation using light-interference measurements. A laminar boundary layer on an unheated, uncooled plate has been shown to cause a refraction error of less than 1 percent for a tunnel 3.6 inches wide if the ratio $\frac{\sqrt{\rho_1 - \rho_w}}{\delta}$ is less than 0.19, where ρ_1 is the density at the edge of the boundary layer, P_w is the density at the surface of the plate, and δ is the boundary-layer thickness. Theoretically, density profiles calculated from interference data can be corrected for refraction effects so as to have a maximum error in the boundary-layer density of a few percent. A comparison between values of the skin-friction coefficient calculated from pressure and from corrected interference measurements shows that the error is generally larger than the theoretically indicated maximum. Because refraction errors are directly proportional to the square of the tunnel span, whereas errors due to end effects are inversely proportional to the span, an optimum tunnel width exists for which the total error caused by both these errors will be a minimum. The tunnel used for this investigation was larger than optimum width.

Density and velocity profiles calculated from total-pressure data were similar in shape to profiles predicted by laminar-boundary-layer theory. Profiles from interference data were in poor agreement with the theory near the edge of the boundary layer. The two methods of measurement had the best mutual agreement at the lowest Reynolds numbers used in the investigation. Total-pressure-tube measurements gave the most reliable value of boundary-layer thickness. Skin-friction coefficients, calculated with the momentum equation, varied inversely with the square root of Reynolds number. The values of the section skin-friction coefficient for a given Reynolds number were higher than for incompressible flow, rather than lower as predicted by theory. Consideration of the leading-edge shock wave offers a possible explanation of this discrepancy. The recovery factor calculated from measured temperature and Mach number showed a tendency to increase with Reynolds number. The values were in the

region of 0.87 to 0.88, which was slightly larger than the value calculated from an integration of the energy equation for a laminar incompressible boundary layer.

Lewis Flight Propulsion Laboratory,
National Advisory Committee for Aeronautics,
Cleveland, Ohio, November 23, 1949.

APPENDIX A

SYMBOLS

The following symbols are used in this report:

C_f section skin-friction coefficient

D_f skin-friction drag force on plate section

F fractional portion of tunnel span between object plane and tunnel window (fig. 8)

k constant ($k = 0.1166$ cu ft/slug for air when $\lambda_0 = 5461$ A)

L span of tunnel

M Mach number

N fringe shift through boundary layer measured from interferogram

N_g fringe shift caused by light striking tunnel window at angle

n refractive index of air

n_g refractive index of tunnel window

P total pressure

Pr Prandtl number

p static pressure

Re_x local stream Reynolds number based on distance x

S length along light path through boundary layer

T total temperature

t ambient-air temperature

u air velocity

x chordwise distance measured from leading edge parallel to stream

y	distance measured perpendicular to plate surface
y'	dy/dz
y''	d^2y/dz^2
z	transverse coordinate between tunnel windows
α	nondimensional coordinate perpendicular to plate surface
β	nondimensional coordinate parallel to plate surface and transverse to stream direction
δ	boundary-layer thickness
δ_g	boundary-layer thickness on tunnel windows
η_t	temperature recovery factor
θ	angle between tangent to light path and plate surface
θ_r	refraction angle of light impinging on tunnel window
λ_0	vacuum wavelength of light
ν_1	stream kinematic viscosity
ρ	air density
$(\rho/\rho_1)_{av}$	density ratio averaged along light path between tunnel windows for two-dimensional-flow field
$(\rho/\rho_1)_{ind}$	density ratio calculated from fringe shift N with equation (4)
τ	thickness of tunnel window

Subscripts:

0	free-stream stagnation conditions
1	conditions at edge of boundary layer
a	conditions at point where light ray appears to originate

av	average
b	average density along light path through boundary layer including side-wall boundary layer
e	condition at point where light path intersects tunnel window nearest camera
f	average density along light path through free stream including side-wall boundary layer
i	conditions at point where light ray is incident on boundary layer
ind	indicated
w	conditions at surface of plate

APPENDIX B

LIGHT PATH AND ERROR CALCULATIONS FOR ASSUMED PROFILE

Equations (5) can be put in the form

$$\frac{d\theta}{dz} = \frac{1}{n}\frac{dn}{dy} \tag{B1}$$

if n is independent of z; θ is the angle that a tangent to a point on the light path makes with the z-axis. By substituting density for refractive index, according to equation (6), and replacing z and y with the nondimensional quantities $\alpha = y/\delta$ and $\beta = z/L$, where δ is the boundary-layer thickness and L the tunnel span, equation (B1) becomes

$$\frac{d^2\alpha}{d\beta^2} = \frac{L^2 k\rho_1}{\delta^2}\frac{d\left(\frac{\rho}{\rho_1}\right)}{d\alpha} \tag{B2}$$

Because θ is small, it has been replaced by dy/dz and $1/n$ has been assumed 1. The assumed density profile is represented by

$$\frac{\rho}{\rho_1} = \frac{1}{2}\left[\left(1 + \frac{\rho_w}{\rho_1}\right) - \left(1 - \frac{\rho_w}{\rho_1}\right)\cos \pi\alpha\right] \tag{B3}$$

where ρ_w is the density at the wall and

$$\frac{d\left(\frac{\rho}{\rho_1}\right)}{d\alpha} = \frac{\pi}{2}\left(1 - \frac{\rho_w}{\rho_1}\right)\sin \pi\alpha \tag{B4}$$

Equation (B4) substituted into equation (B2) gives the differential equation for the light path.

$$\frac{d^2\alpha}{d\beta^2} = \frac{L^2 k\pi(\rho_1 - \rho_w)}{2\delta^2}\sin \pi\alpha = K \sin \pi\alpha \tag{B5}$$

When integrated once, equation (B5) yields

$$\frac{d\alpha}{d\beta} = \sqrt{\frac{2K}{\pi}}\left(\pi c_1 - \cos \pi\alpha\right)^{1/2} \tag{B6}$$

If the light enters the tunnel parallel to the surface of the plate, $\frac{dy}{dz} = \frac{\delta}{L}\frac{d\alpha}{d\beta} = 0$ when $\alpha = \alpha_i$, the initial height of the light on entering the tunnel. By replacing the constant of integration c_1 in equation (B6) and integrating again,

$$\beta = \sqrt{\frac{\pi}{2K}}\int_{\alpha_i}^{\alpha} \frac{d\alpha}{\sqrt{\cos \pi\alpha_i - \cos \pi\alpha}} \tag{B7}$$

where

$$\alpha \geq \alpha_i$$

This equation is an elliptic integral of the first kind, which has been evaluated for a number of values of α_i and is plotted in figure 26 in terms of α and $\sqrt{\pi K}\beta$. From this information, α_e and θ_e, the height above the surface and the angle of the light when it leaves the tunnel, respectively, were obtained as functions of α_i for a free-stream total pressure of 30 inches mercury absolute, and a free-stream total temperature of 560° R; that is, $\rho_1 = 5.15 \times 10^{-5}$ slugs per cubic foot, $\rho_w/\rho_1 = 0.584$, $\delta = 0.028$ inch, and $L = 3.60$ inches. Curves showing α_e and θ_e are presented in figure 27. The apparent height at which each light ray appears to originate was calculated from θ_e and α_e for two locations of the object plane, one on the center line of the plate, the other at the edge of the plate nearest the light source, from the equation

$$y_a = \delta\alpha_e - \left(FL + \tau\frac{n_g - 1}{n_g}\right)\theta_e \tag{B8}$$

where F is determined by the location of the object plane. The indicated density was found by numerically summing the density along each light path to obtain the average density traversed by the ray and then adding the term $\frac{\lambda_0}{\rho_1 kL} N_g$ due to the fringe shift when the light passes through the tunnel window at an angle. The indicated profiles focused on the two planes and the original assumed profile are shown in figure 11.

The manner in which the error between the indicated and assumed profiles varies through the boundary layer is plotted in figure 10. The total error is composed of the three errors previously discussed in Refraction errors. Each of these errors was evaluated from the light-path calculations in order to show the individual contributions to the total error.

The averaging error was found by subtracting the numerically calculated average density along a light path from the density at the incident height of the light. Thus the averaging error is

$$\left(\frac{\rho}{\rho_1}\right)_{av} - \left(\frac{\rho}{\rho_1}\right)_i \tag{B9}$$

The window error caused by the light striking the tunnel window at an angle makes the indicated density $\left(\frac{\rho}{\rho_1}\right)_{ind}$ higher than the average density. The measured fringe shift N, used to calculate the indicated density, will be less by an amount N_g than the fringe shift required to indicate a density $\left(\frac{\rho}{\rho_1}\right)_{av}$. Therefore,

$$\left(\frac{\rho}{\rho_1}\right)_{av} = 1 - \frac{\lambda_0}{kL\rho_1}(N + N_g)$$

or

$$\left(\frac{\rho}{\rho_1}\right)_{ind} - \left(\frac{\rho}{\rho_1}\right)_{av} = \frac{\lambda_0}{\rho_1 kL} N_g \tag{11}$$

which can be used to calculate the window error by using the appropriate value of N_g corresponding to the emergent angle of the light.

The displacement error is given by the difference between the densities at the incident height and the height y_a from which the light appears to originate. The sign of the error

$$\left(\frac{\rho}{\rho_1}\right)_i - \left(\frac{\rho}{\rho_1}\right)$$

depends on whether y_a is greater or less than y_i.

Summing the expressions for the three errors yields the identity

$$\left(\frac{\rho}{\rho_1}\right)_{ind} - \left(\frac{\rho}{\rho_1}\right) \equiv \left[\left(\frac{\rho}{\rho_1}\right)_{av} - \left(\frac{\rho}{\rho_1}\right)_i\right] + \left[\left(\frac{\rho}{\rho_1}\right)_{ind} - \left(\frac{\rho}{\rho_1}\right)_{av}\right] + \left[\left(\frac{\rho}{\rho_1}\right)_i - \left(\frac{\rho}{\rho_1}\right)\right] \tag{B10}$$

APPENDIX C

DERIVATION OF AVERAGE-DENSITY AND EMERGENT-HEIGHT EQUATIONS FOR CONSTANT DENSITY GRADIENT

Equation (5) can be put in the form

$$\frac{d\theta}{dz} = \frac{1}{n}\frac{dn}{dy} \tag{B1}$$

Rewriting this expression in terms of density by means of equation (6), including the assumption that $1/n = 1$, leads to a differential equation that can be integrated for a constant density gradient, giving

$$\theta = k\frac{d\rho}{dy}z \tag{C1}$$

where the boundary conditions at the point of entrance of the light ray are $\theta = 0^{\circ}$ and $z = 0$. Because θ will be small, $\tan\theta = \theta = dy/dz$. Equation (C1), when integrated again, becomes

$$y - y_i = \frac{1}{2}k\frac{d\rho}{dy}z^2 \tag{C2}$$

The light ray enters the tunnel at the height y_i at $z = 0$ and leaves at y_e at $z = L$. Under the assumption of a linear density change from y_e to y_i, the density gradient can be expressed as

$$\frac{d\rho}{dy} = \rho_1\frac{\left(\frac{\rho}{\rho_1}\right)_e - \left(\frac{\rho}{\rho_1}\right)_i}{y_e - y_i} \tag{C3}$$

Substituting equation (C3) in equation (C2) and evaluating at $z = L$ gives

$$(y_e - y_i)^2 = \frac{1}{2}k\rho_1 L^2\left[\left(\frac{\rho}{\rho_1}\right)_e - \left(\frac{\rho}{\rho_1}\right)_i\right] \tag{9}$$

The average density along a light path is

$$\rho_{av} = \frac{1}{S}\int_0^S \rho(S)\ dS \tag{C4}$$

Inasmuch as $dS = dz\sqrt{1 + y'^2} = dz\sqrt{1 + \theta^2}$, and θ^2 is negligible compared to unity, dS can be replaced with dz. The assumption of constant density gradient is expressed in the following equation:

$$\rho(y) = \rho_w + \frac{d\rho}{dy}\ y \tag{C5}$$

When rewritten as a function of z using equation (C2), equation (C5) becomes

$$\rho(z) = \rho_w + \frac{d\rho}{dy}\ y_i + \frac{1}{2}\ k\left(\frac{d\rho}{dy}\right)^2 z^2 \tag{C6}$$

(Note that $\rho_w + \frac{d\rho}{dy}\ y_i$ is equivalent to ρ_i.) Substituting this expression for density variation along the light path in equation (C4) and integrating yields

$$\left(\frac{\rho}{\rho_1}\right)_{av} = \left(\frac{\rho}{\rho_1}\right)_i + \frac{1}{6}\ k\rho_1 L^2\left[\frac{d\left(\frac{\rho}{\rho_1}\right)}{dy}\right]^2 \tag{C7}$$

which can be rearranged into equation (8) using equation (C3).

REFERENCES

1. Groth, Eric: Evaluation of Interferometer Measurements on an Aerofoil in the 250 × 250 mm High Speed Tunnel A7. Reps. and Trans. No. 128, AGD 1028, British M.A.P. (Völkenrode), Feb. 1946.

2. Kennard, R. B.: An Optical Method for Measuring Temperature Distribution and Convective Heat Transfer. Bur. Standards Jour. Res., vol. 8, no. 5, May 1932, pp. 787-805.

3. Zobel, Th.: Flow Measurement by Means of Light Interference. NACA TM 1253, 1949.

4. Eckert, Ernest R. G., Drake, R. M., Jr., and Soehngen, Eric: Manufacture of a Zehnder-Mach Interferometer. Tech. Rep. 5721, Air Materiel Command (Wright-Patterson Air Force Base), Aug. 31, 1948. (Available from CADO as ATI 34235.)

5. Gooderun, Paul B., Wood, George P., and Brevoort, Maurice J.: Investigation with an Interferometer of the Turbulent Mixing of a Free Supersonic Jet. NACA TN 1857, 1949.

6. Chapman, Dean R., and Rubesin, Morris W.: Temperature and Velocity Profiles in the Compressible Laminar Boundary Layer with Arbitrary Distribution of Surface Temperature. Jour. Aero. Sci., vol. 16, no. 9, Sept. 1949, pp. 547-565.

7. Bershader, Daniel: An Interferometric Study of Supersonic Channel Flow. Rev. Sci. Instruments, vol. 20, no. 4, April 1949, pp. 260-275.

8. Goldstein, Sidney: Modern Developments in Fluid Dynamics. Vol. II. Clarendon Press (Oxford), 1938, p. 627.

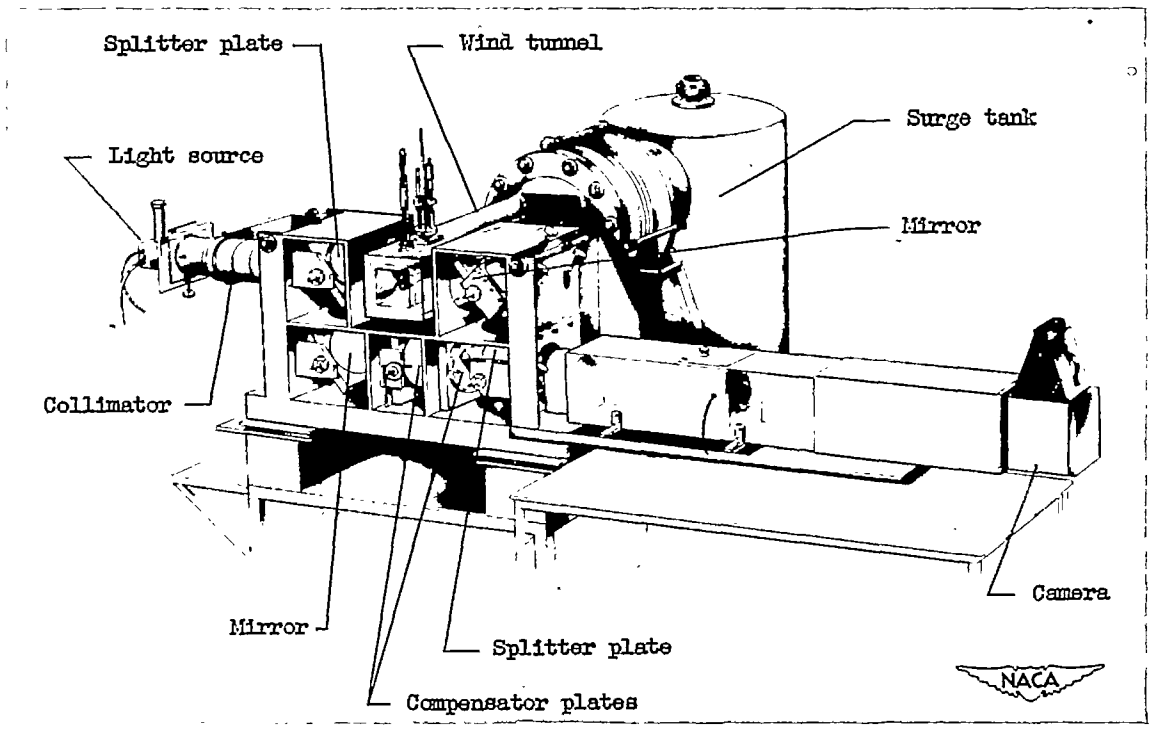

Figure 1. - Interferometer and wind-tunnel installation.

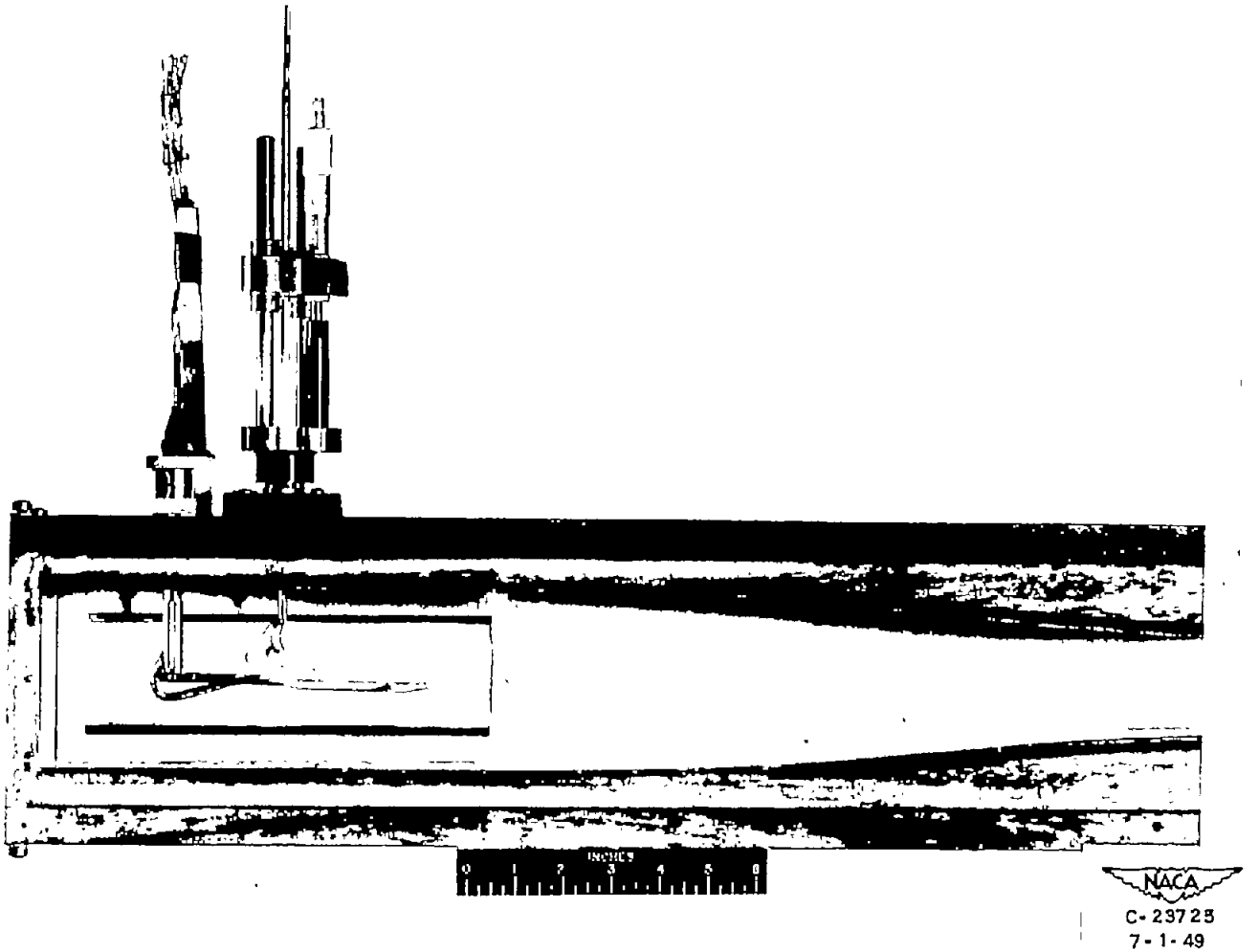

Figure 2. - Wind tunnel and flat plate with one side plate removed.

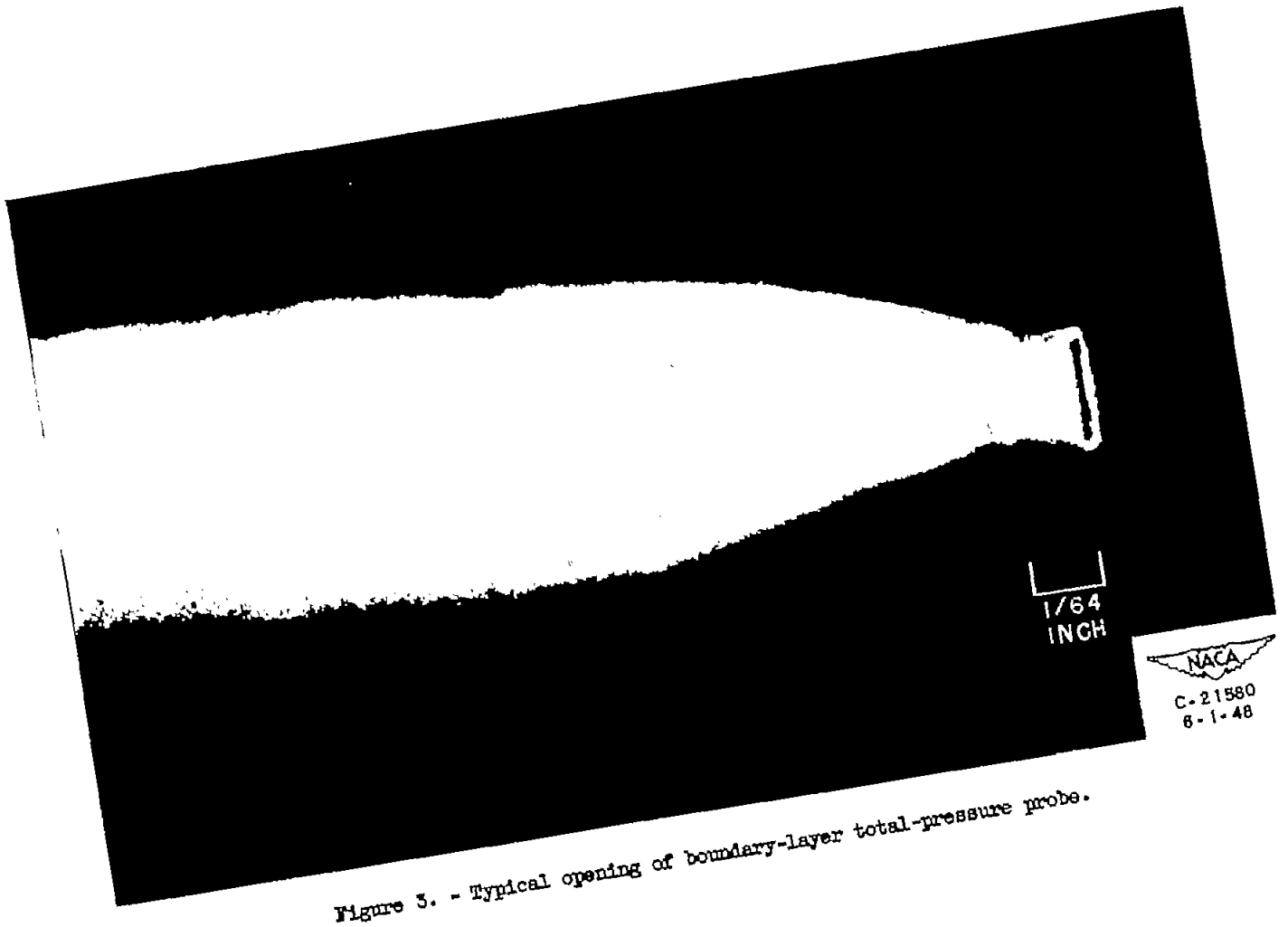

Figure 3. - Typical opening of boundary-layer total-pressure probe.

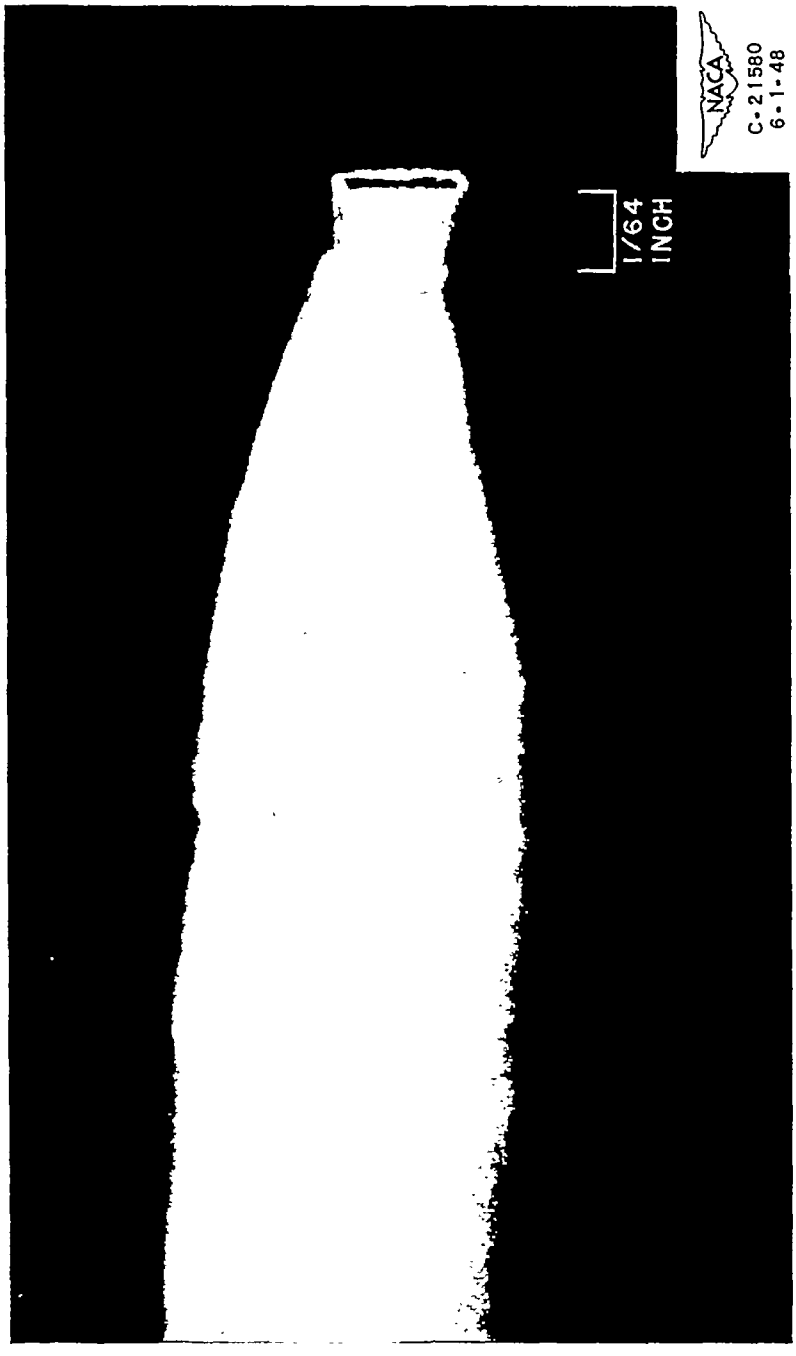

Figure 3. - Typical opening of boundary-layer total-pressure probe.

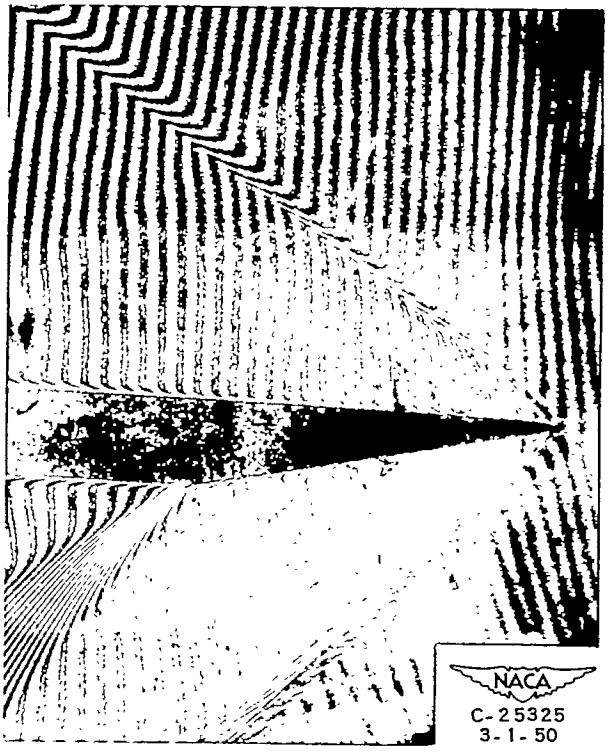

Figure 4. - Leading-edge shock wave.

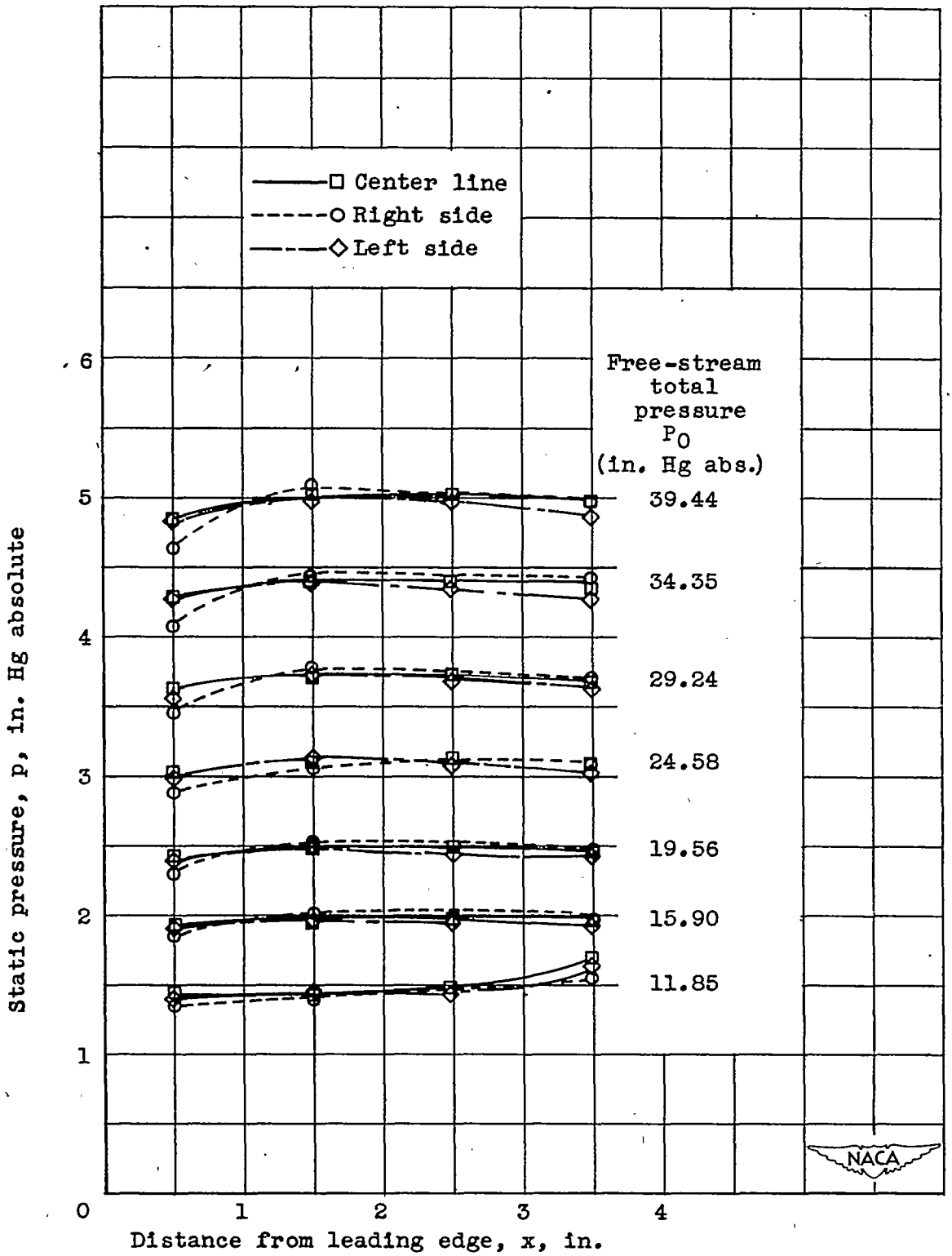

Figure 5. - Pressure distribution on plate at various inlet pressures and free-stream total temperature of 560° R.

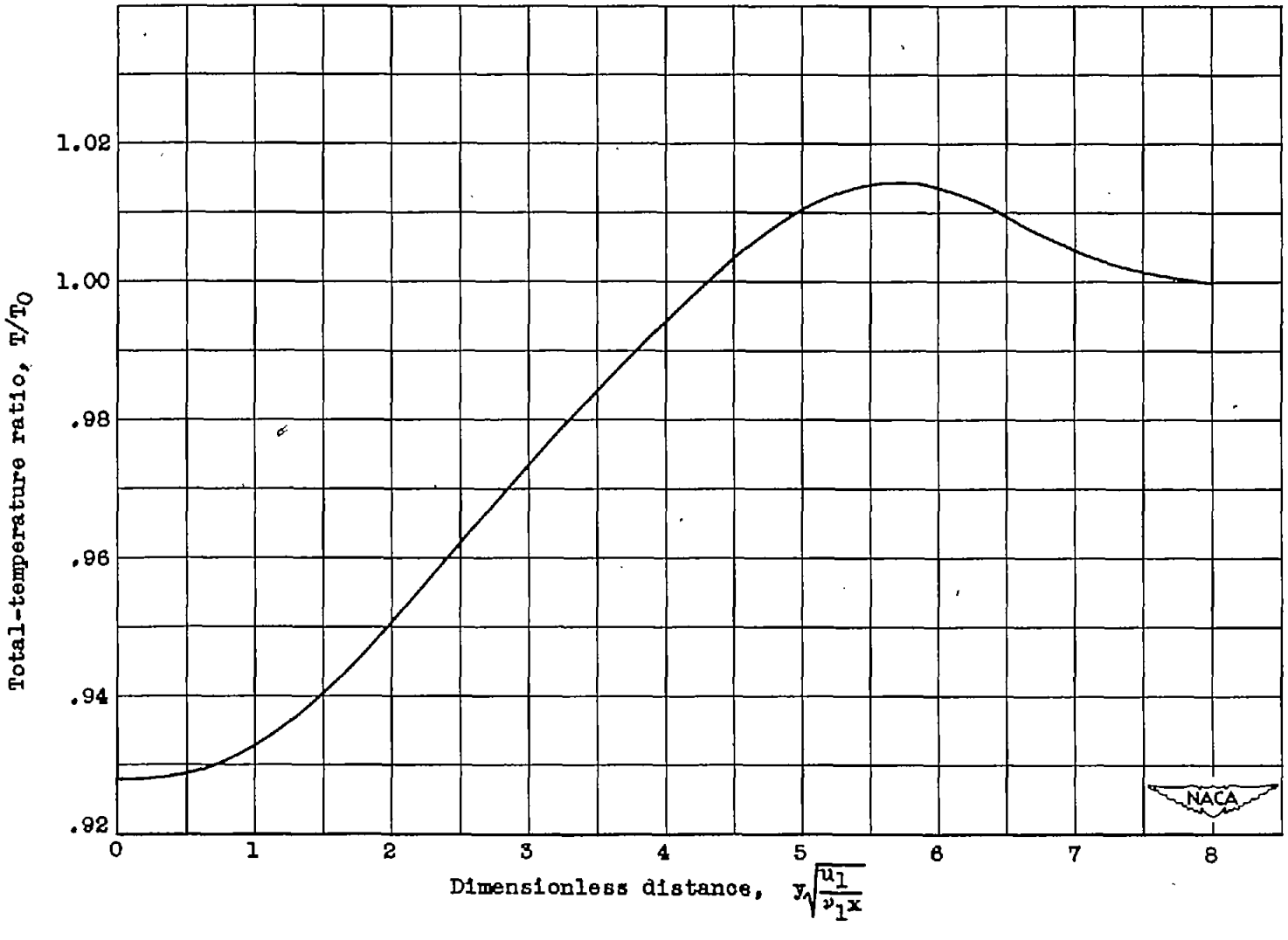

Figure 6. - Boundary-layer total-temperature distribution calculation from theory of reference 6. Mach number at edge of boundary layer, 2.09.

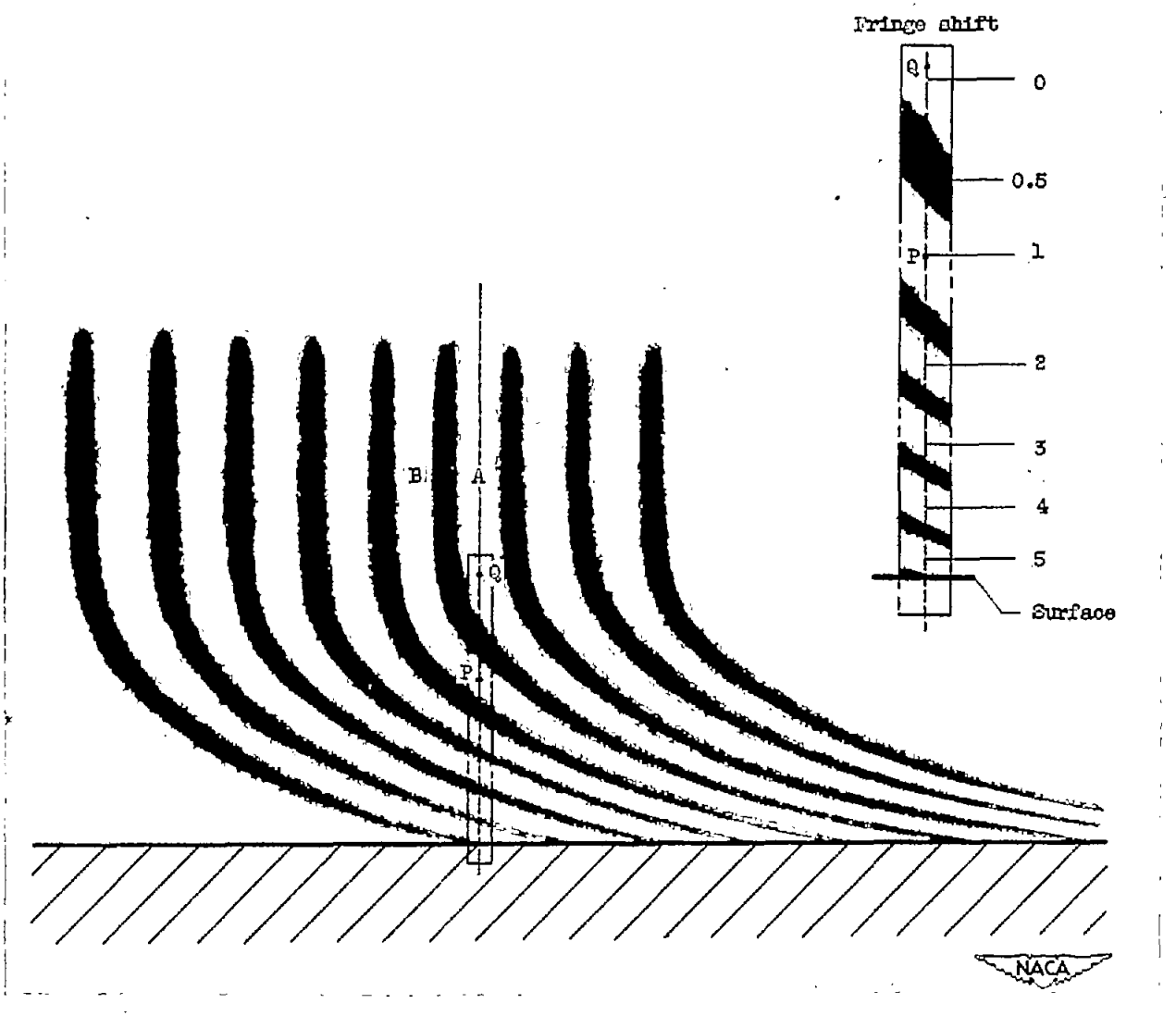

Figure 7. - Illustration of method for analysis of interference data.

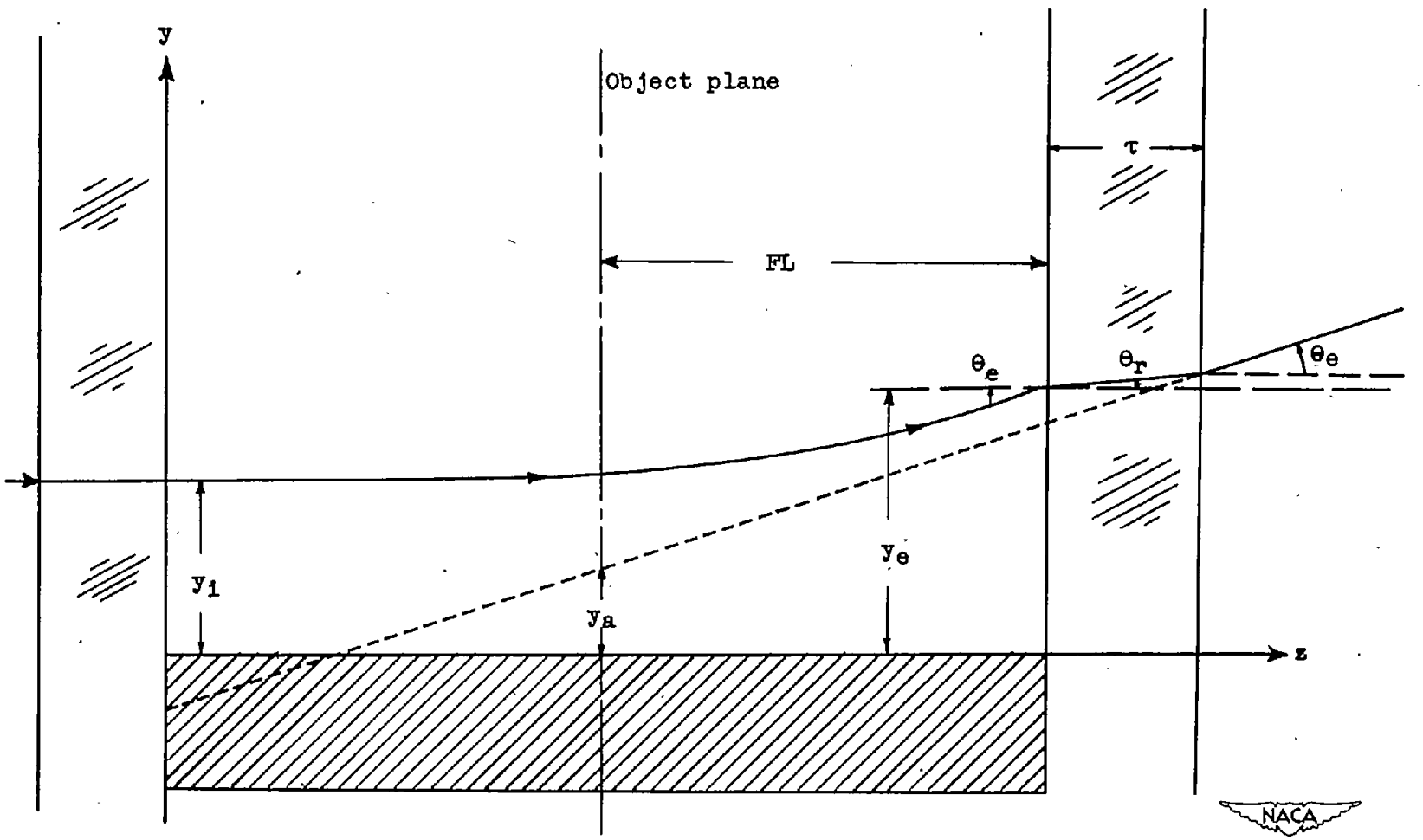

Figure 8. - Schematic diagram of light path through boundary layer.

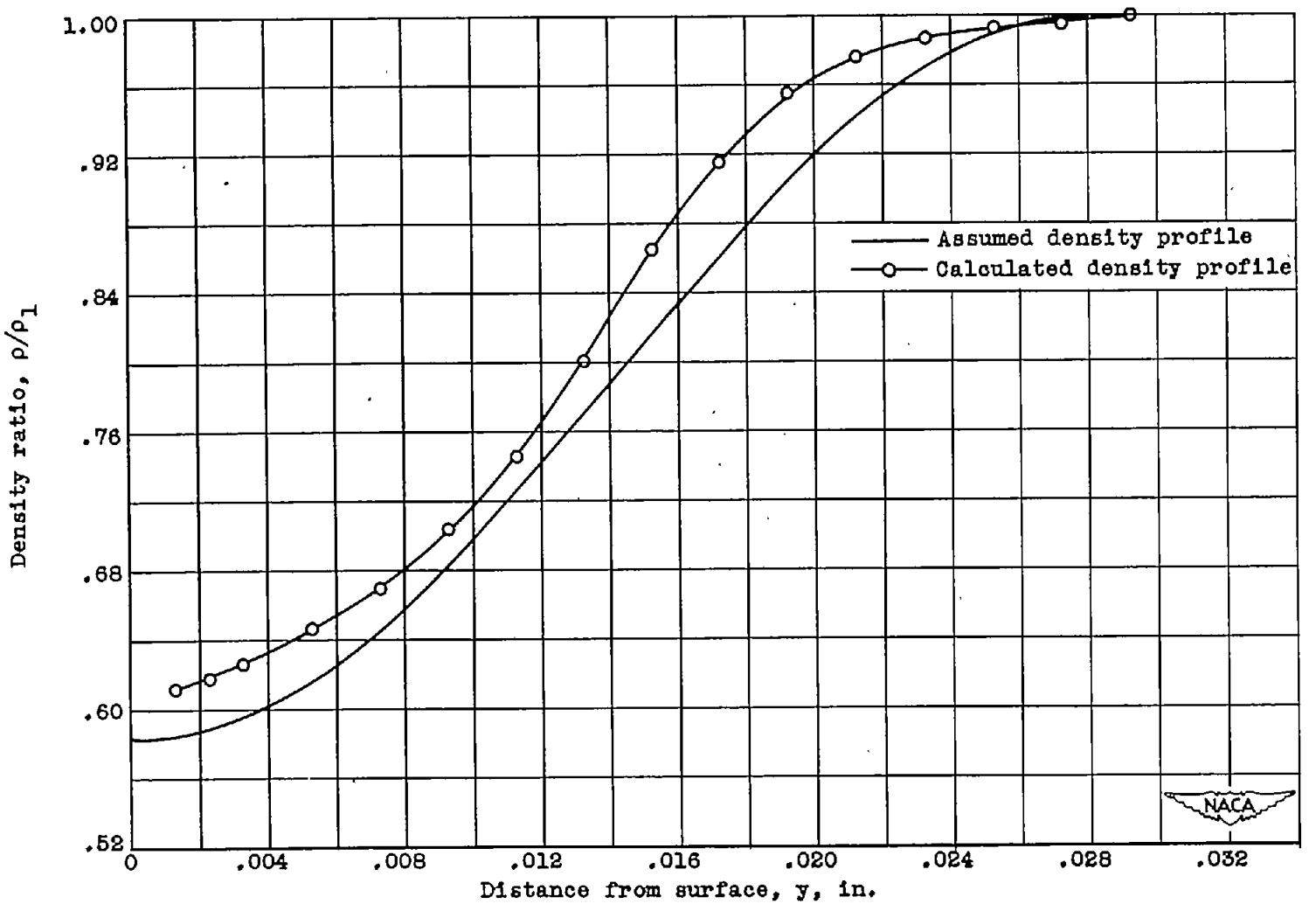

Figure 9. - Comparison of measured and assumed density profile used for refraction calculations. Free-stream total pressure, 30.00 inches mercury absolute; free-stream total temperature, 560° R; Mach number at boundary-layer edge, 2.01; local stream Reynolds number, 0.759×10^6.

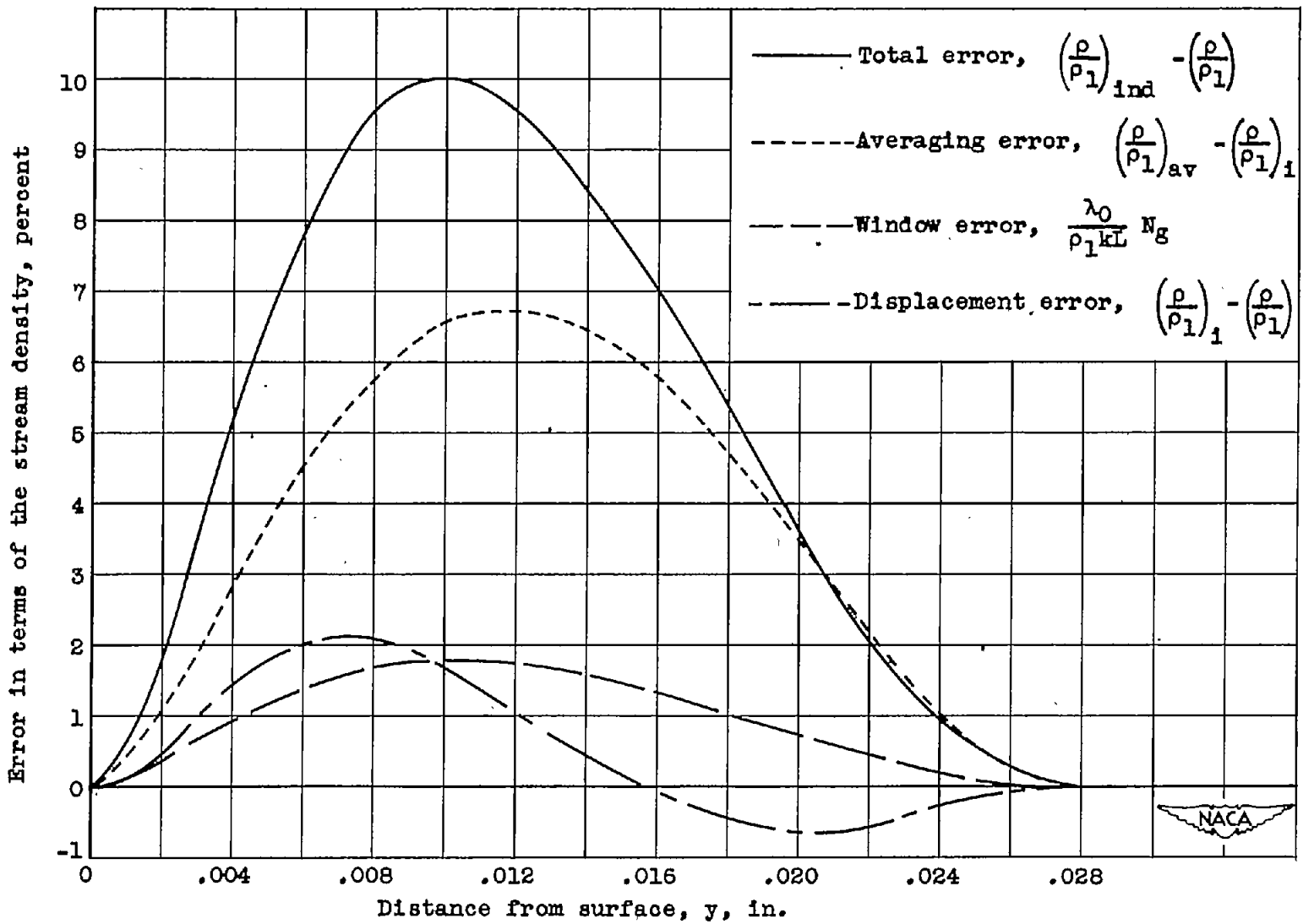

Figure 10. - Variation of refraction errors through assumed boundary-layer profile.

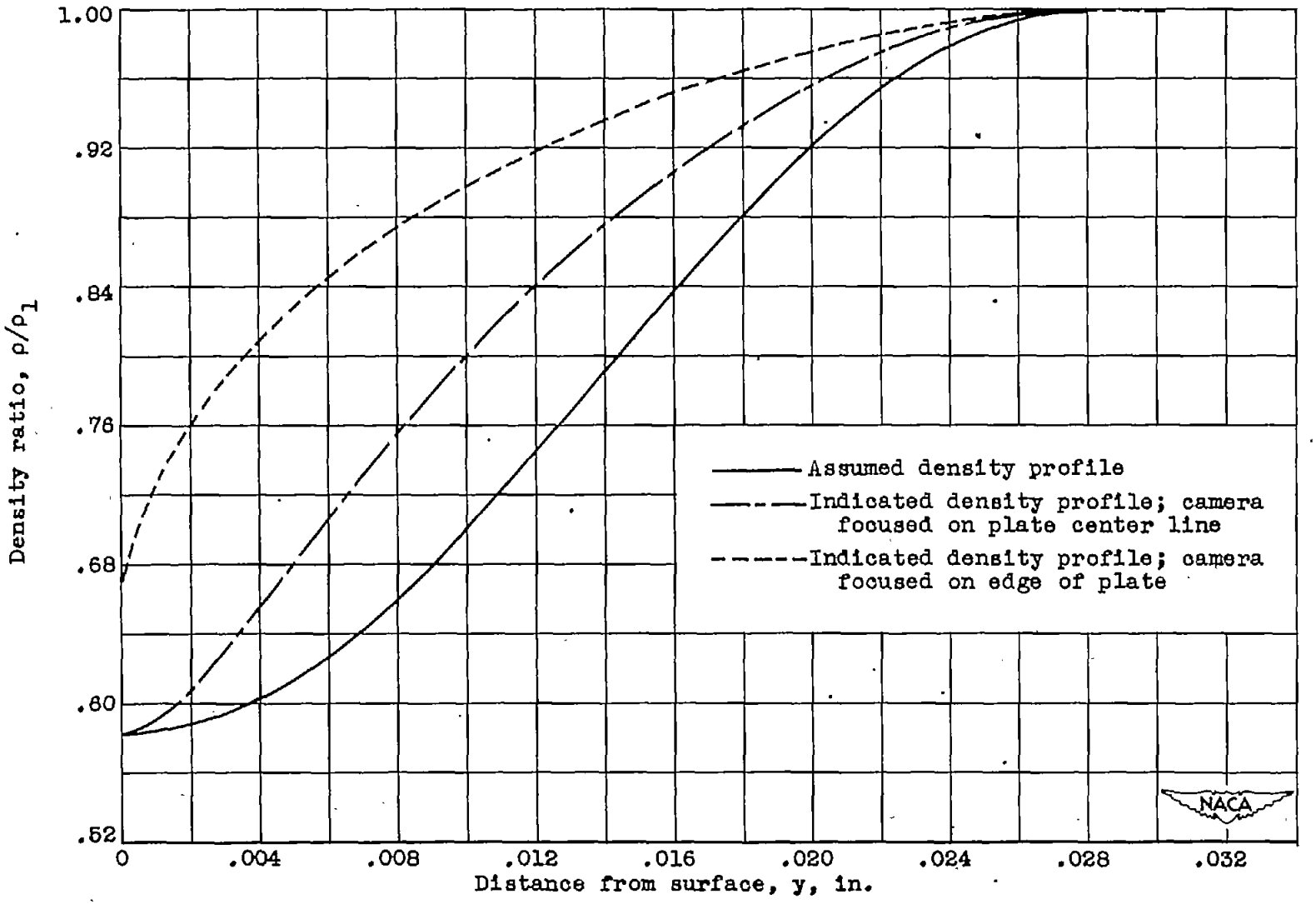

Figure 11. - Comparison of indicated and assumed density profiles.

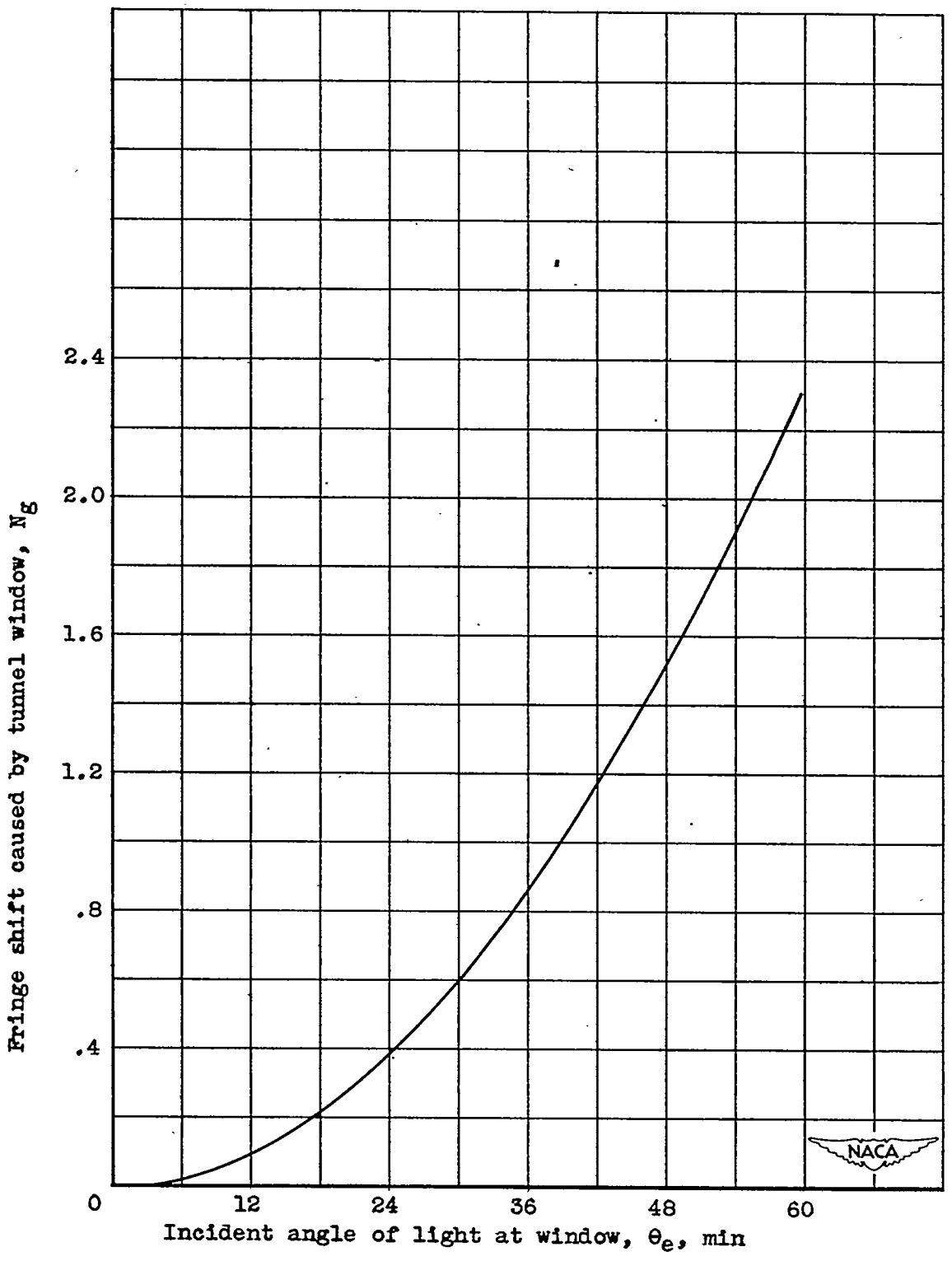

Figure 12. - Fringe shift caused by light striking 1/2-inch thickness of crown glass (n_g = 1.52) at an angle.

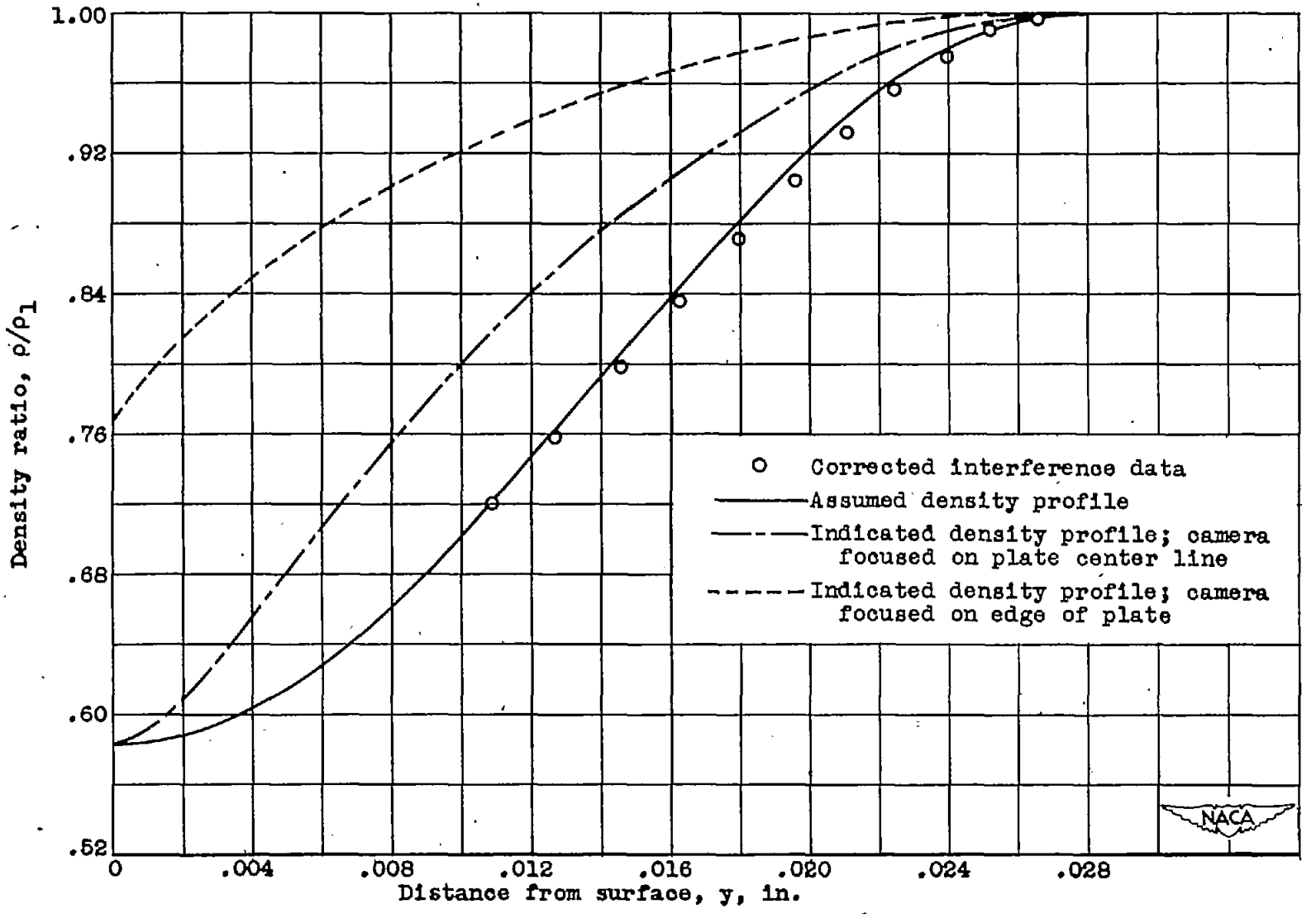

Figure 13. - Comparison of corrected interference data with assumed density profile.

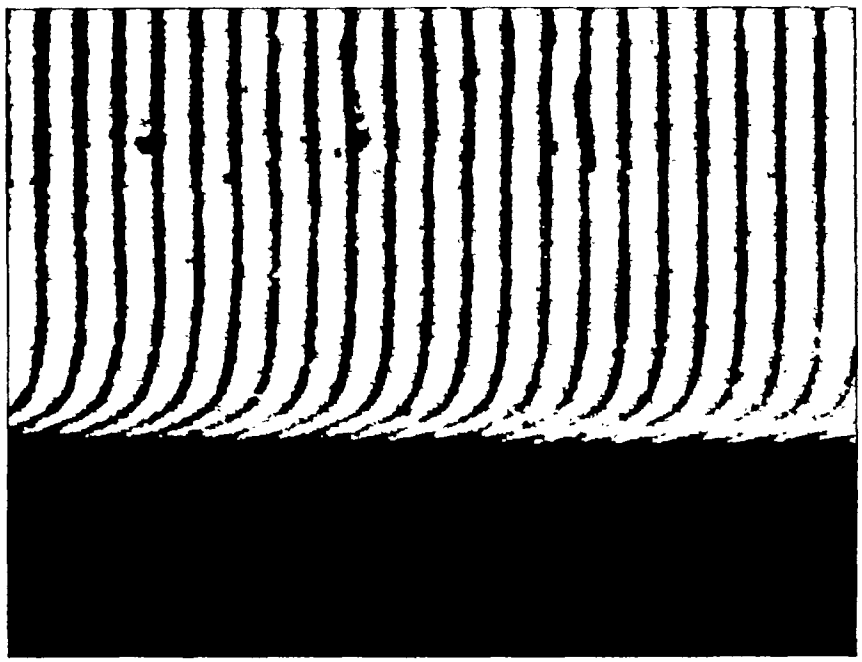

(a) Double exposure.

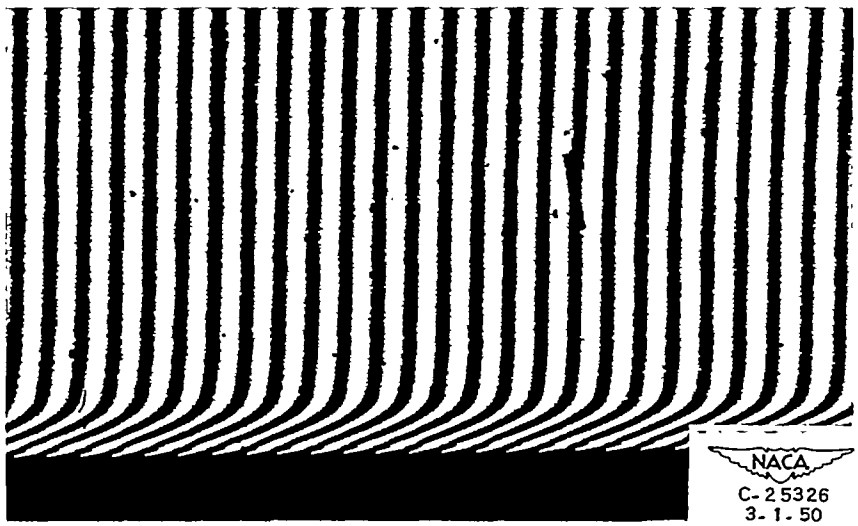

(b) Single exposure.

Figure 14. - Interferograms illustrating apparent downward shift of surface when camera is focused on edge of plate.

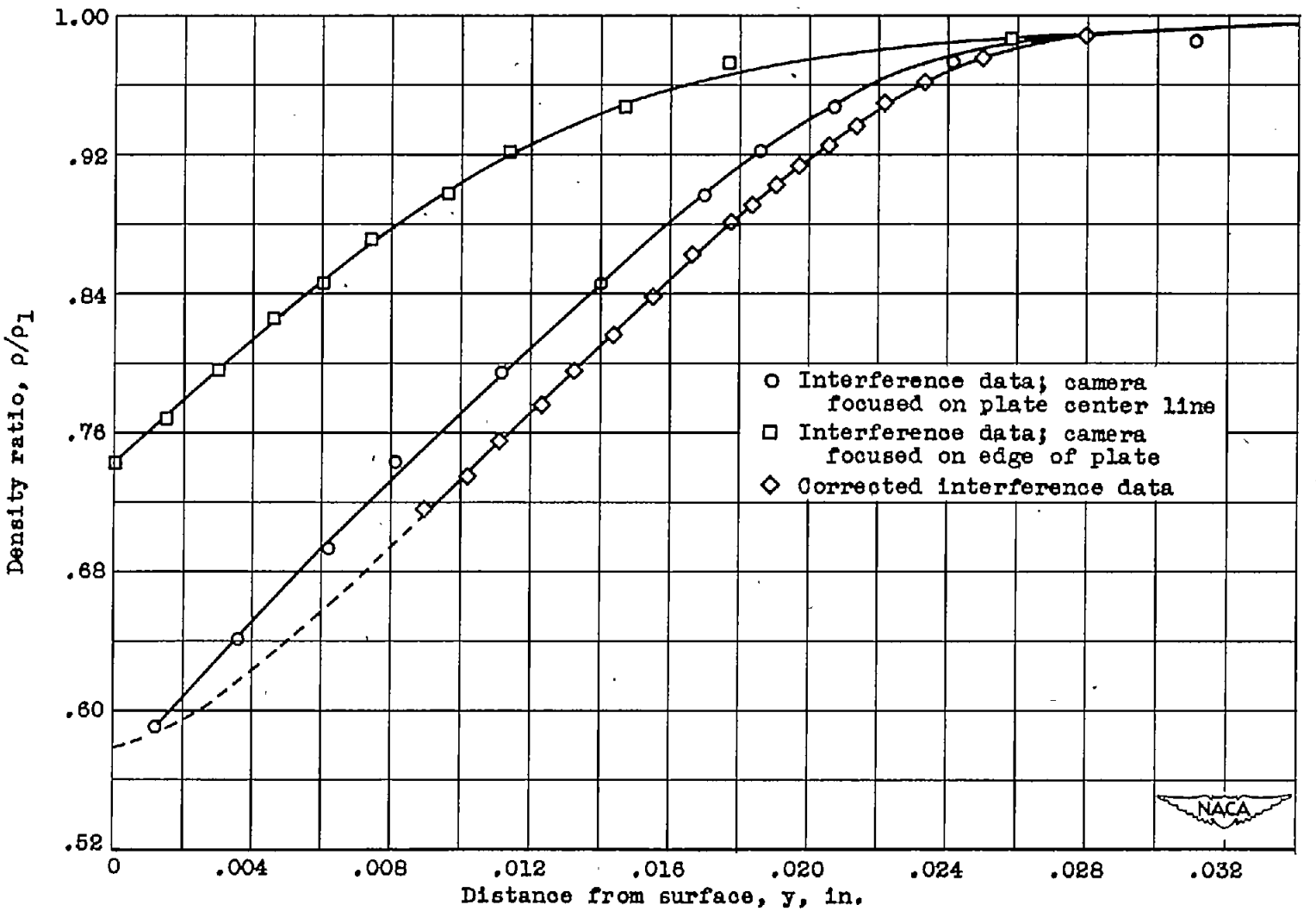

Figure 15. - Comparison of indicated and corrected density profiles. Free-stream total pressure, 29.33 inches mercury absolute; free-stream total temperature, 560° R; Mach number at boundary-layer edge, 2.04; local stream Reynolds number, 0.730×10^6.

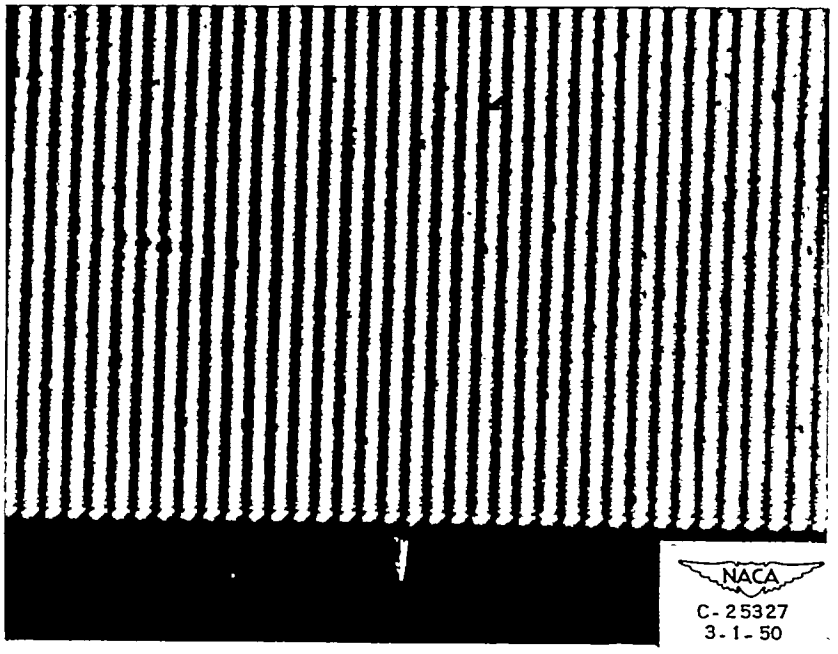

Figure 16. - No-flow interference photograph showing poor definition of plate surface.

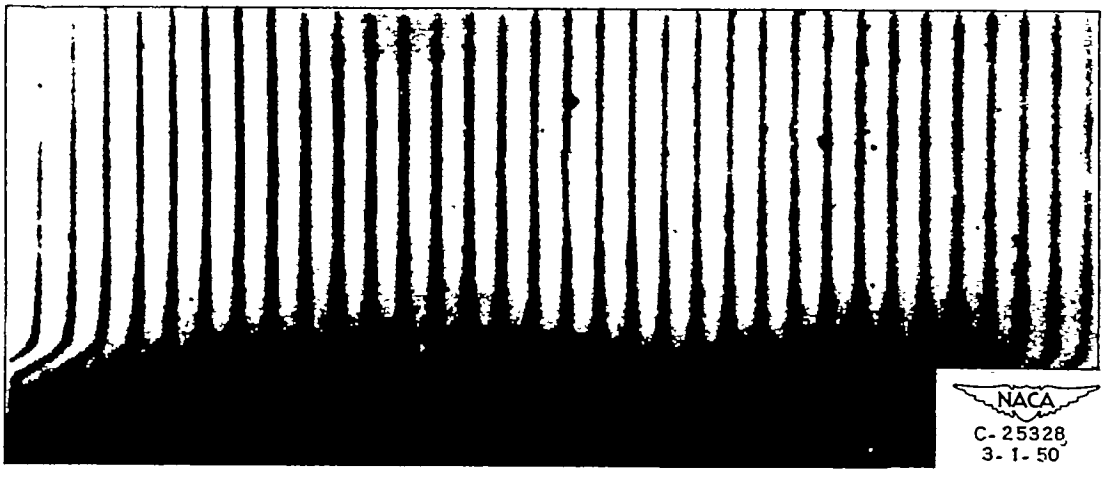

Figure 17. - Interference photograph illustrating unequal thickness of dark and light fringes caused by overdeveloping.

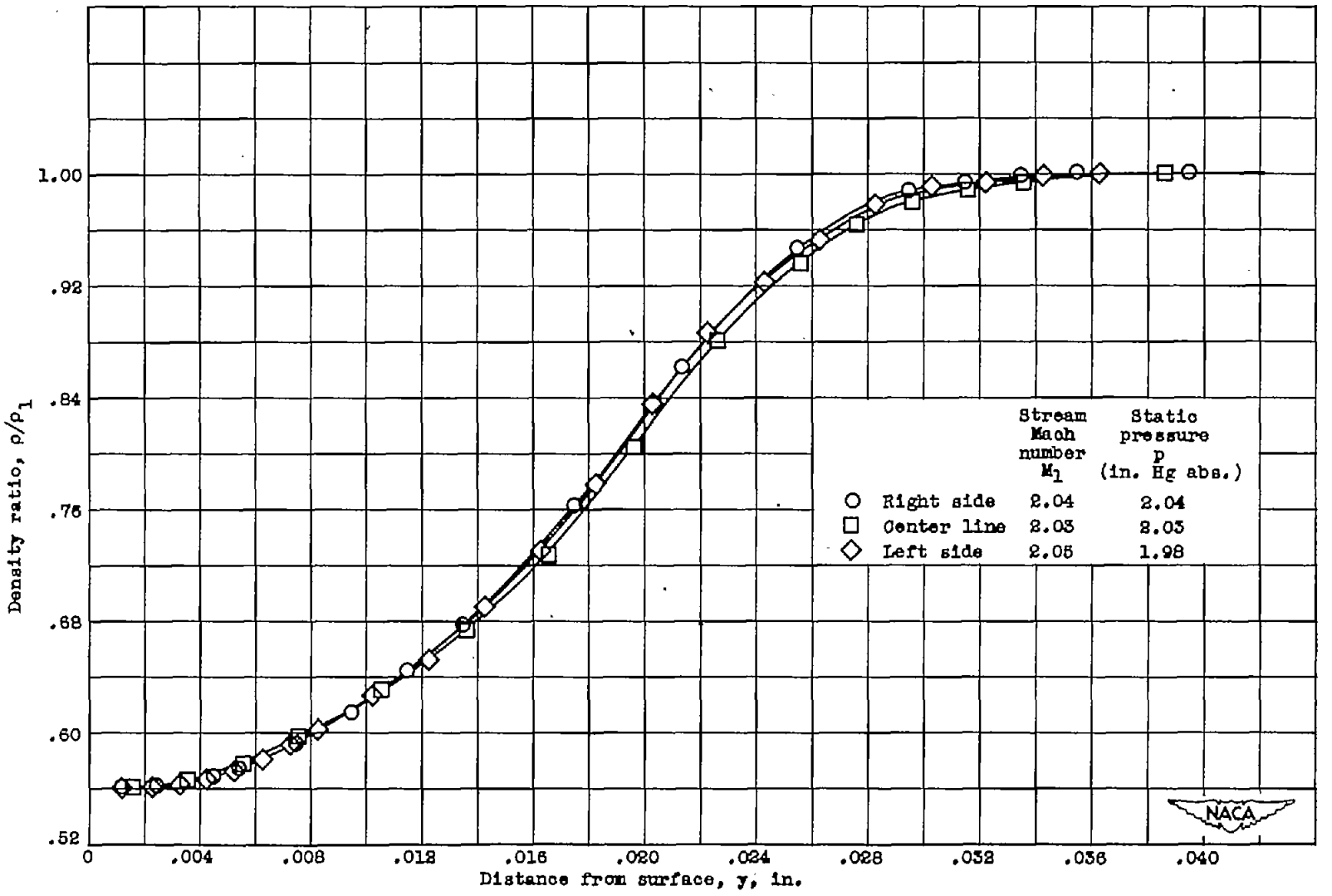

(a) Reynolds number, 0.388×10^6.

Figure 18. - Comparison of density profiles at three spanwise positions.

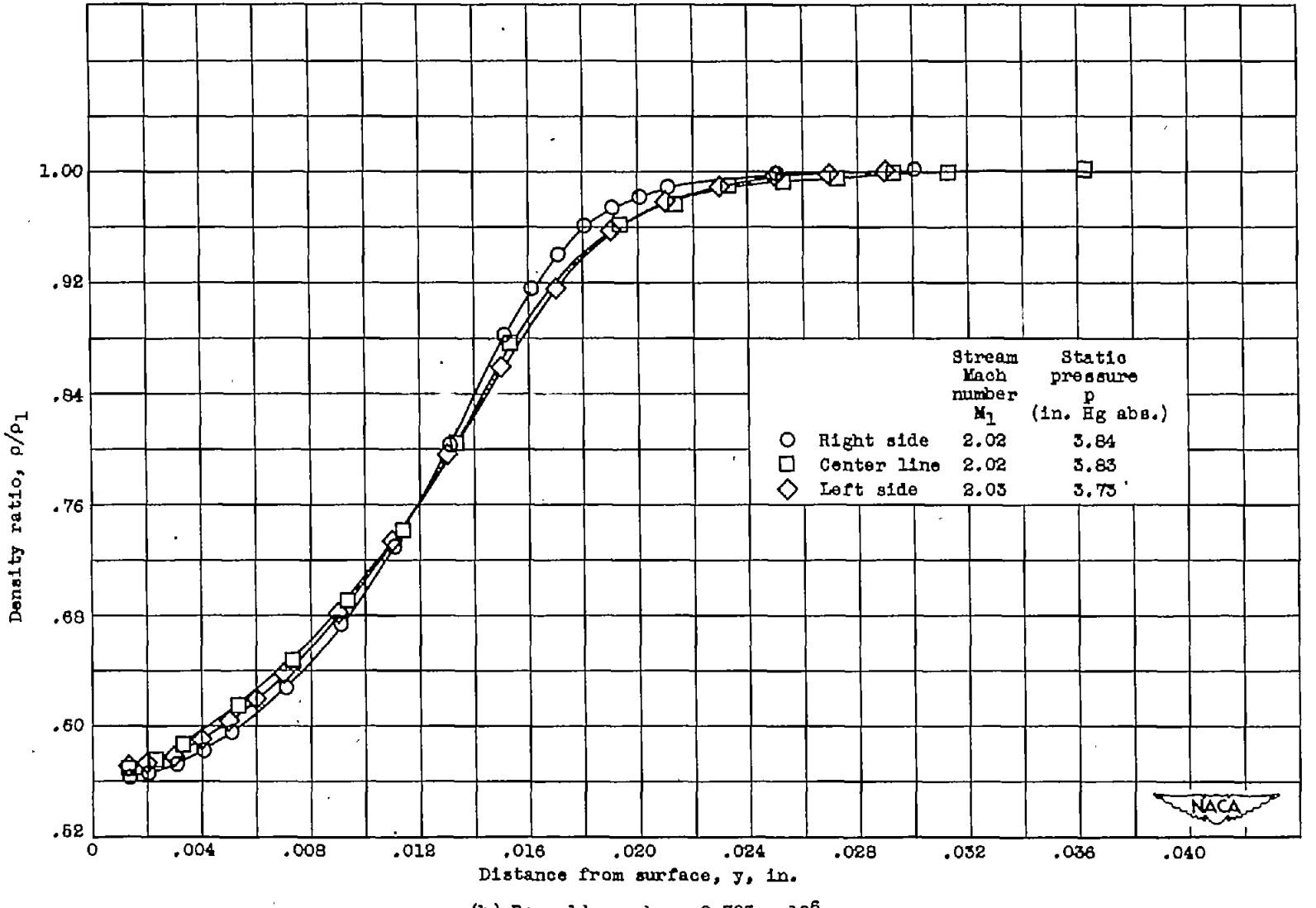

(b) Reynolds number, 0.783×10^6.

Figure 18. - Continued. Comparison of density profiles at three spanwise positions.

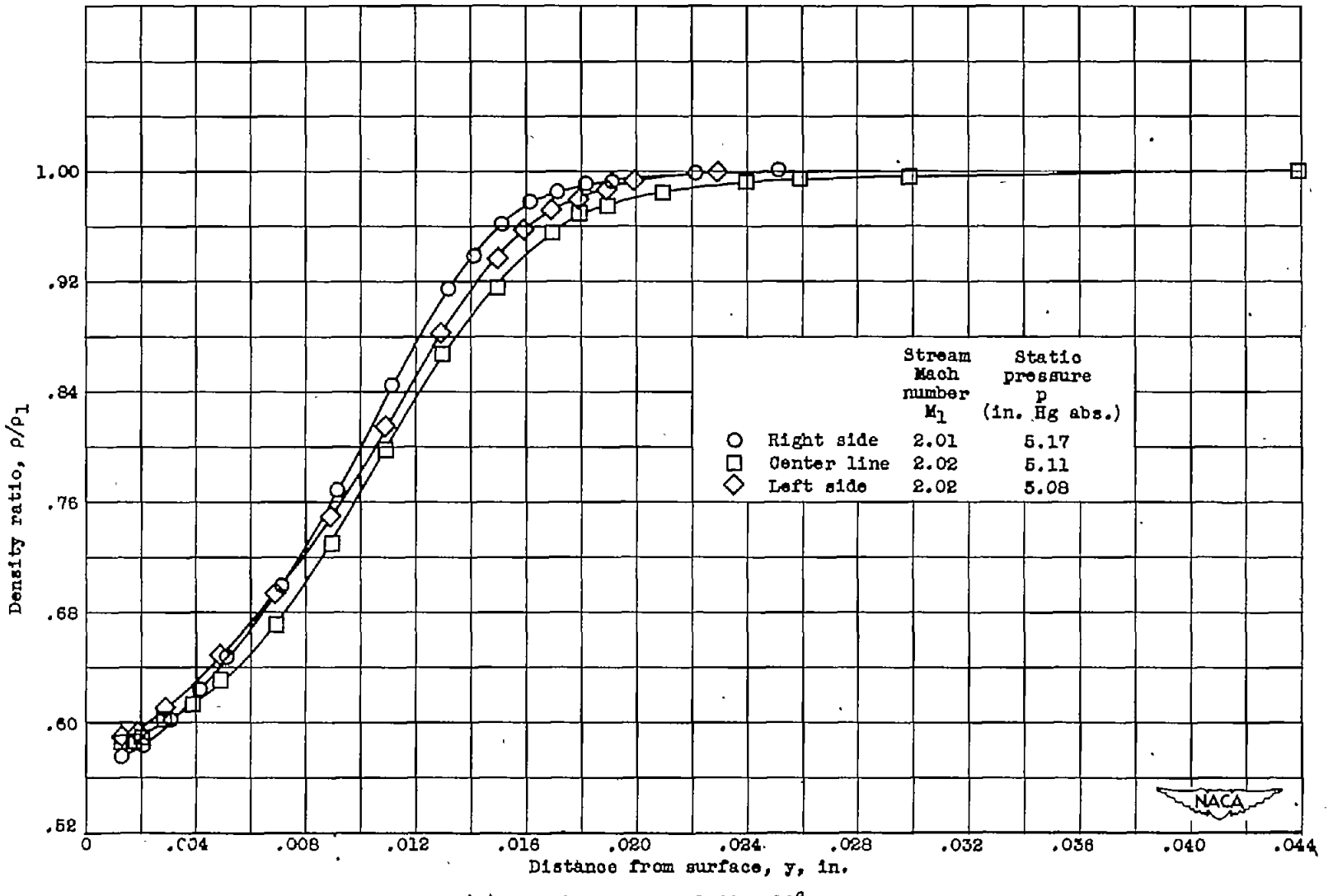

(c) Reynolds number, 1.09×10^6.

Figure 18. - Concluded. Comparison of density profiles at three spanwise positions.

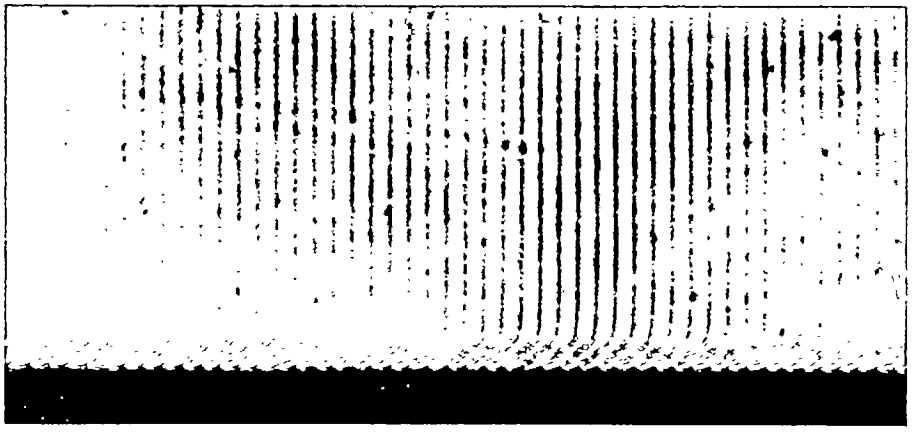

(a) Free-stream total pressure, 15.93 inches mercury; stream Mach number 2.06; Reynolds number, 0.384×10^6.

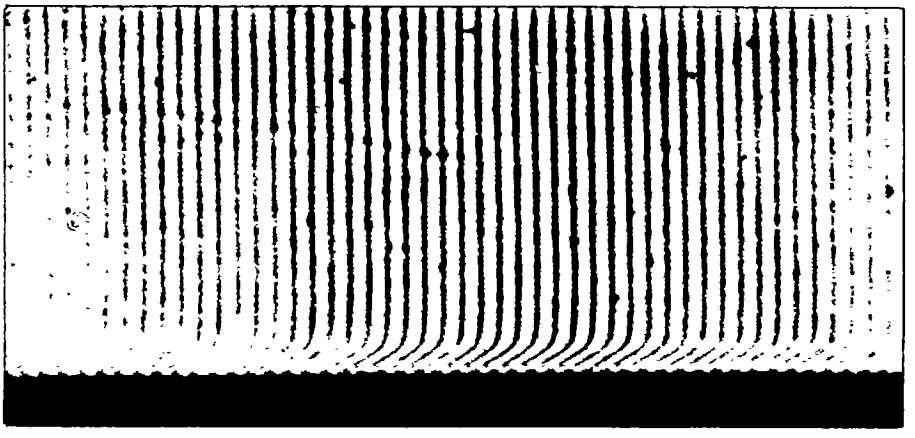

(b) Free-stream total pressure, 19.52 inches mercury; stream Mach number, 2.05; Reynolds number, 0.483×10^6.

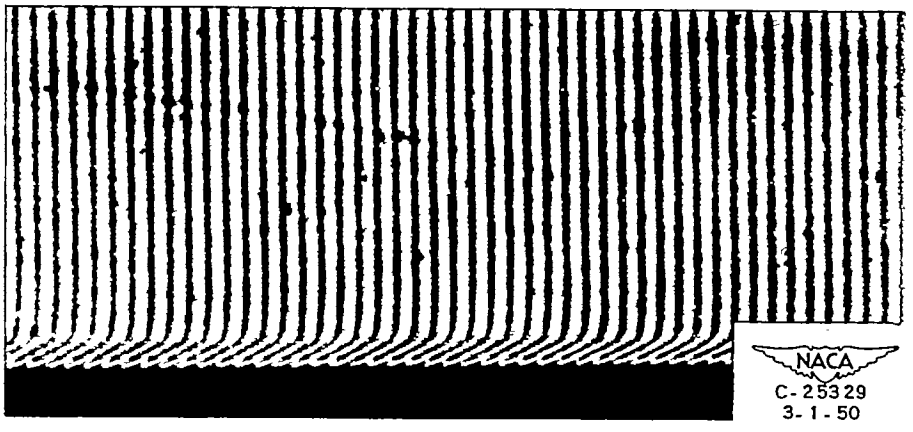

(c) Free-stream total pressure, 24.71 inches mercury; stream Mach number, 2.05; Reynolds number, 0.611×10^6.

Figure 19. - Interference photographs for six Reynolds numbers taken with camera focused on tunnel center line. Free-stream total temperature, 560° R.

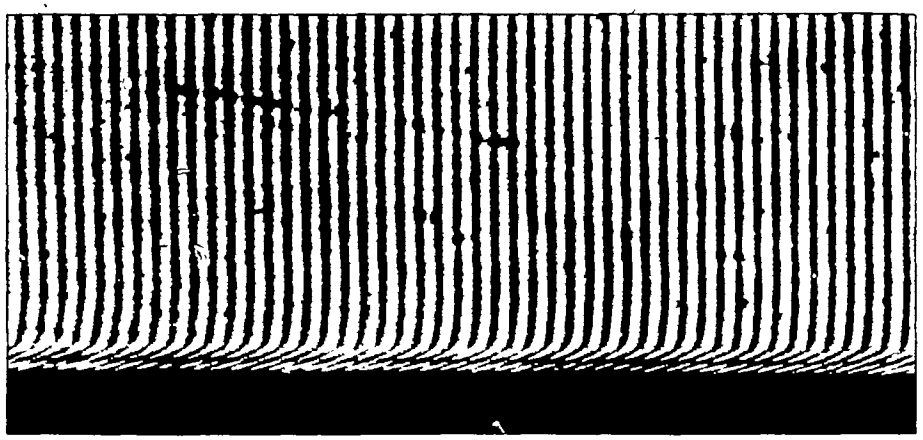

(d) Free-stream total pressure, 29.33 inches mercury; stream Mach number, 2.04; Reynolds number, 0.730×10^6.

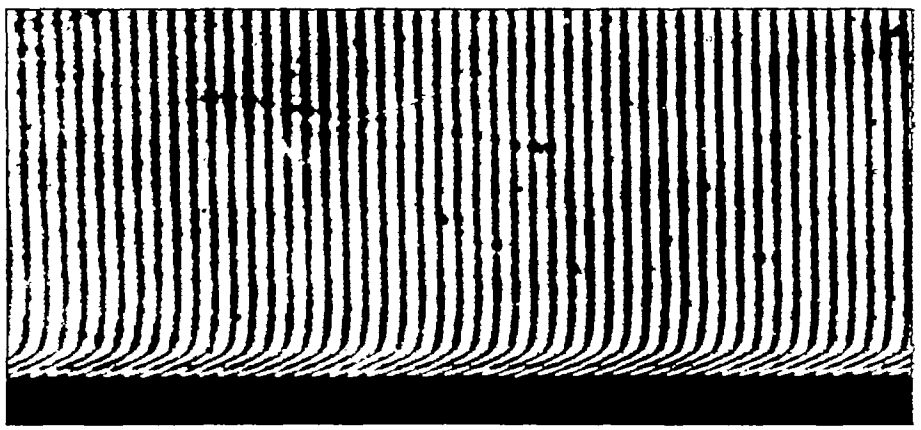

(e) Free-stream total pressure, 34.41 inches mercury; stream Mach number, 2.03, Reynolds number, 0.858×10^6.

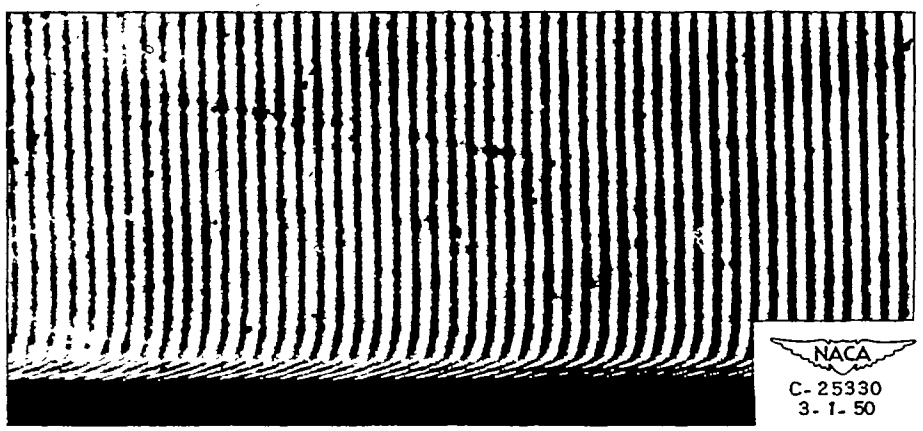

(f) Free-stream total pressure, 39.55 inches mercury; stream Mach number, 2.02; Reynolds number, 0.989×10^6.

Figure 19. - Concluded. Interference photographs for six Reynolds numbers taken with camera focused on tunnel center line. Free-stream total temperature, 560° R.

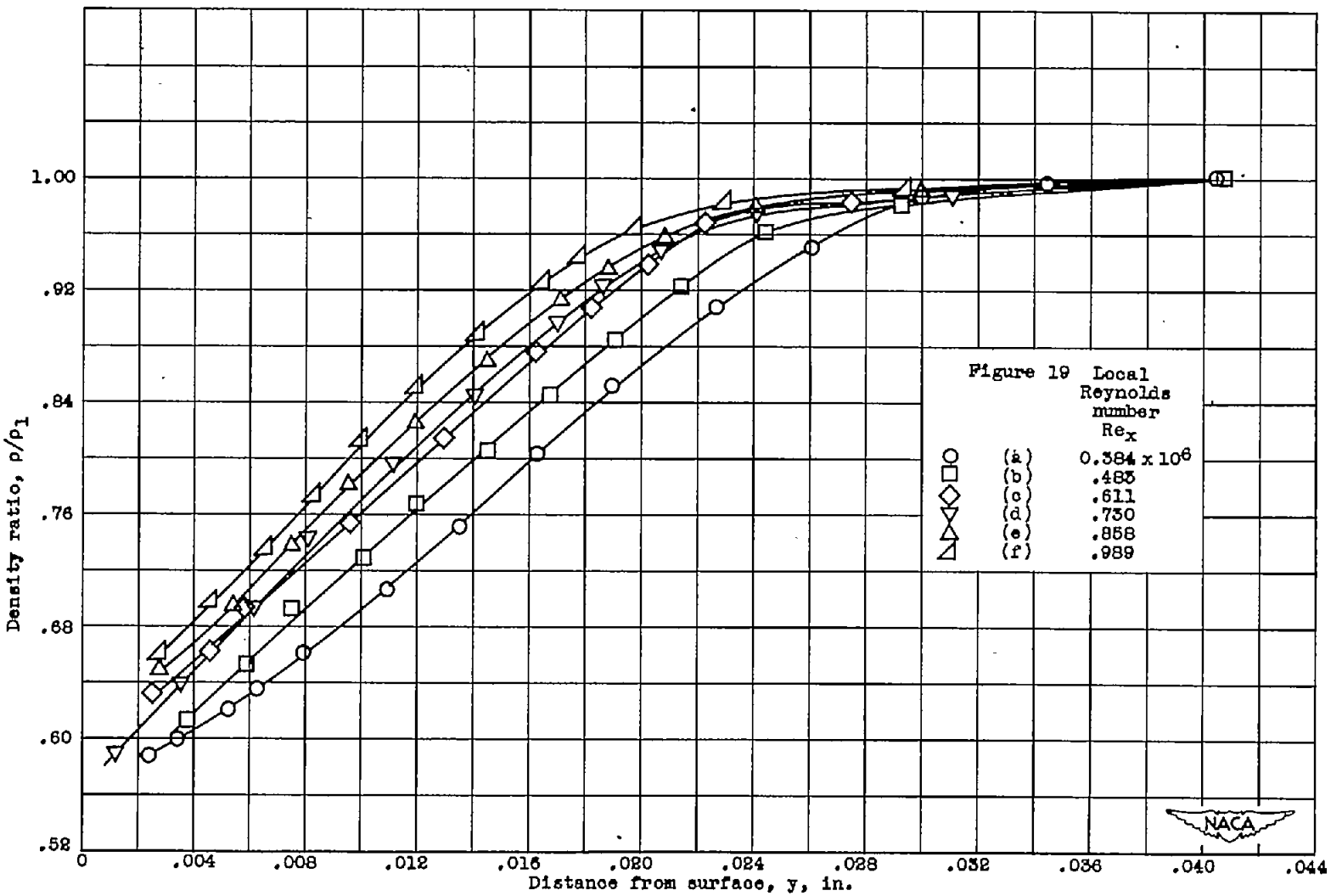

(a) Indicated profiles $2\frac{1}{2}$ inches from leading edge. Taken from interferograms of figure 19.

Figure 20. - Density profiles.

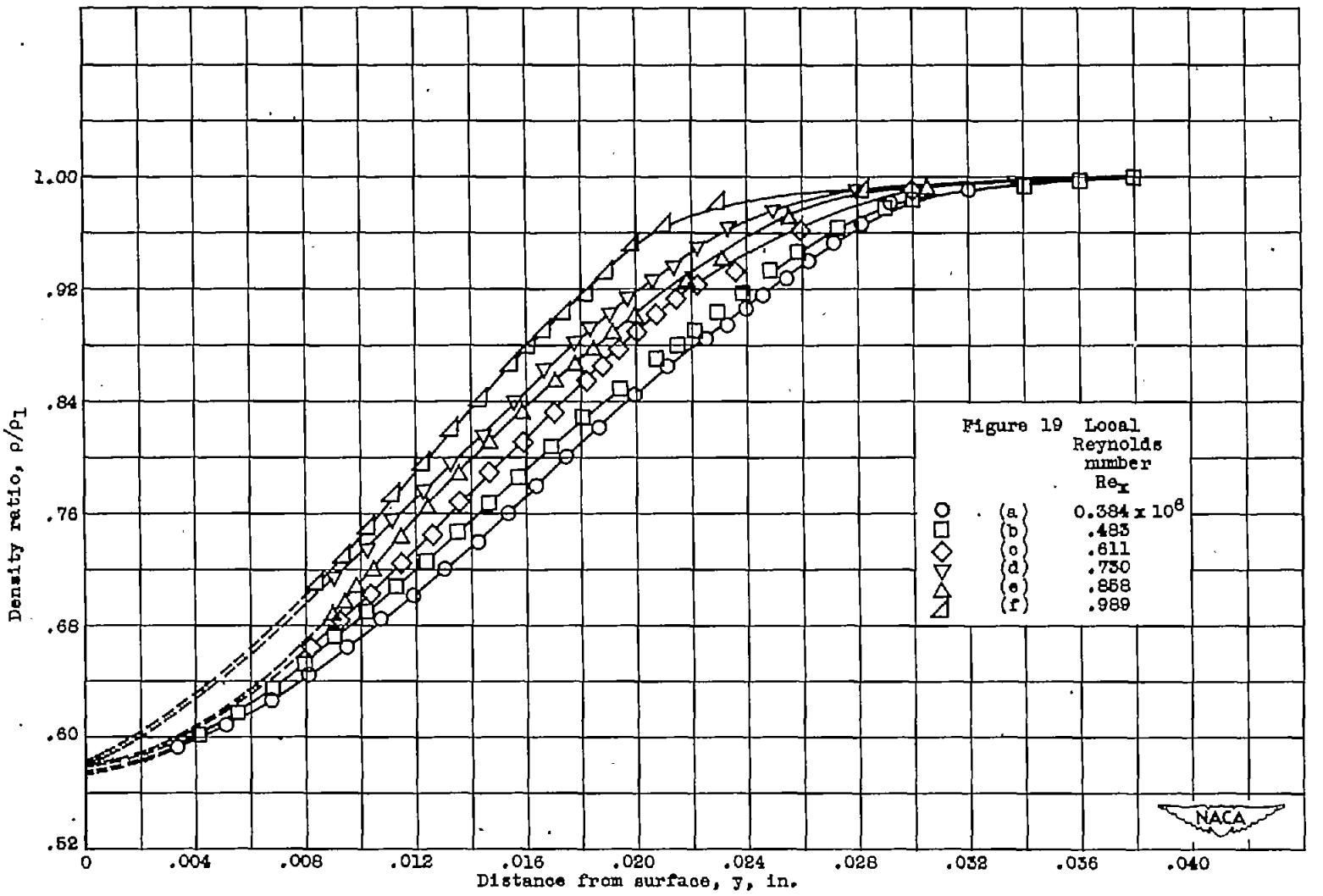

(b) Corrected profiles corresponding to indicated profiles of figure 20(a).

Figure 20. - Concluded. Density profiles.

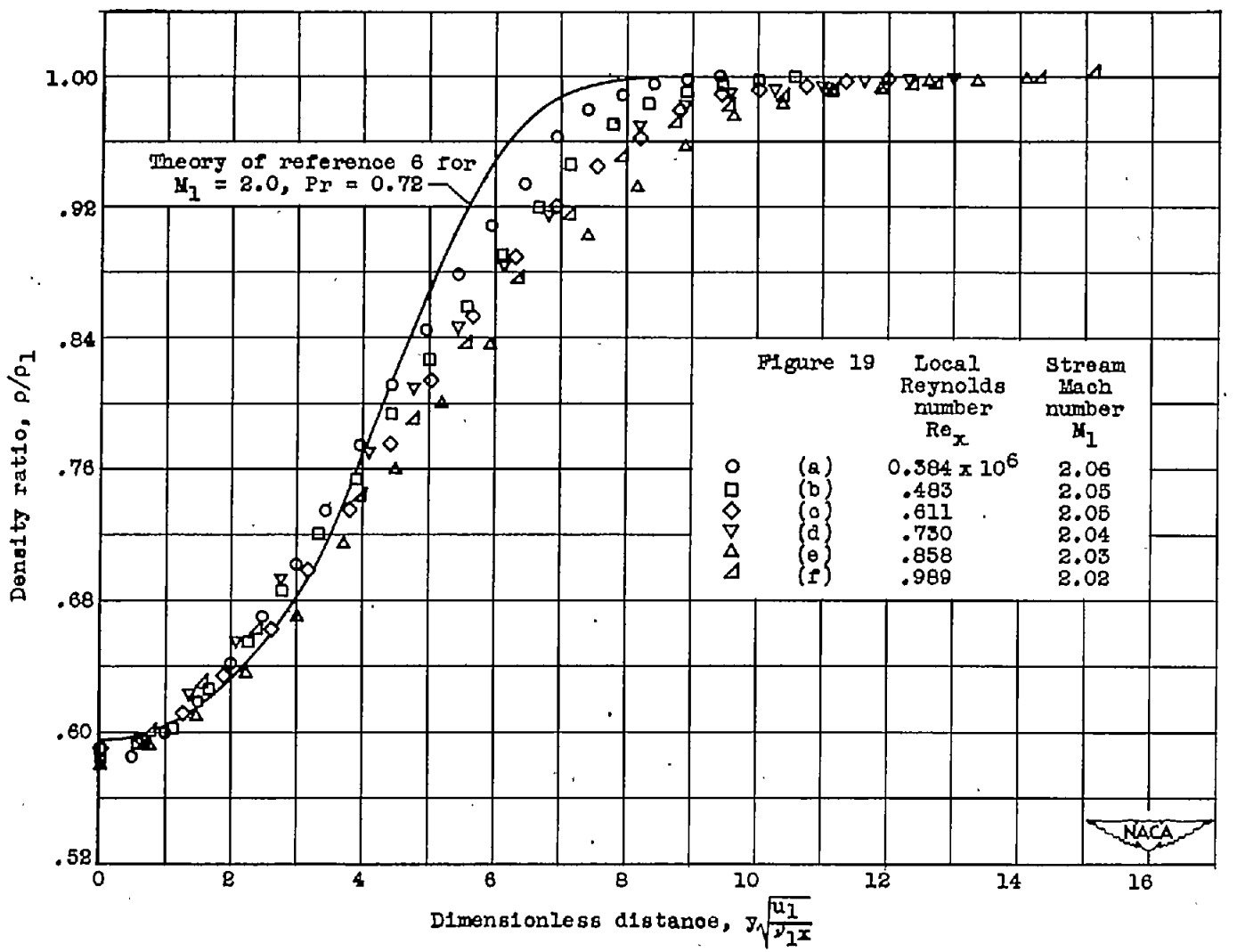

(a) Interference measurements.

Figure 21. - Density profiles from interference and total-pressure measurements.

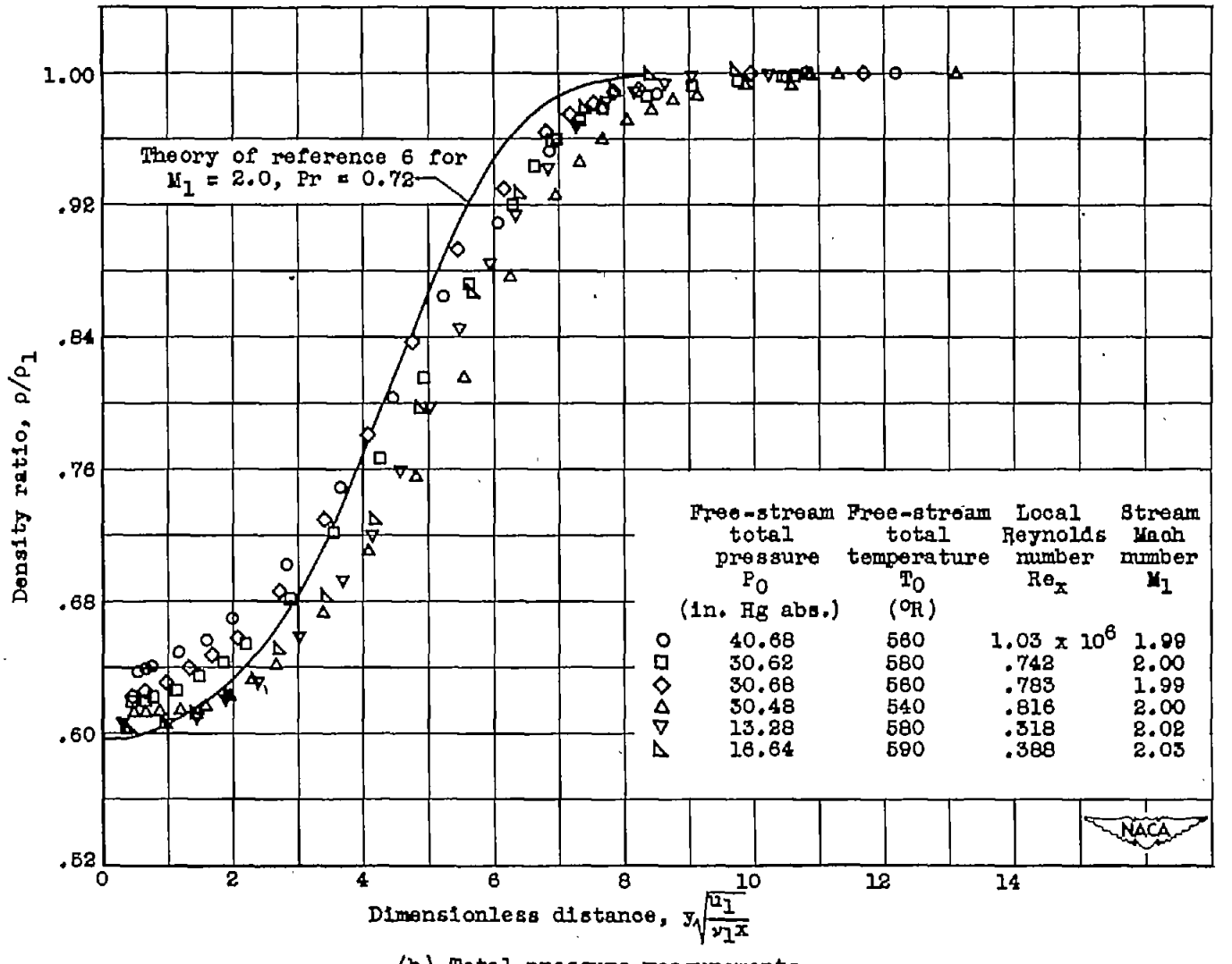

(b) Total-pressure measurements.

Figure 21. - Concluded. Density profiles from interference and total-pressure measurements.

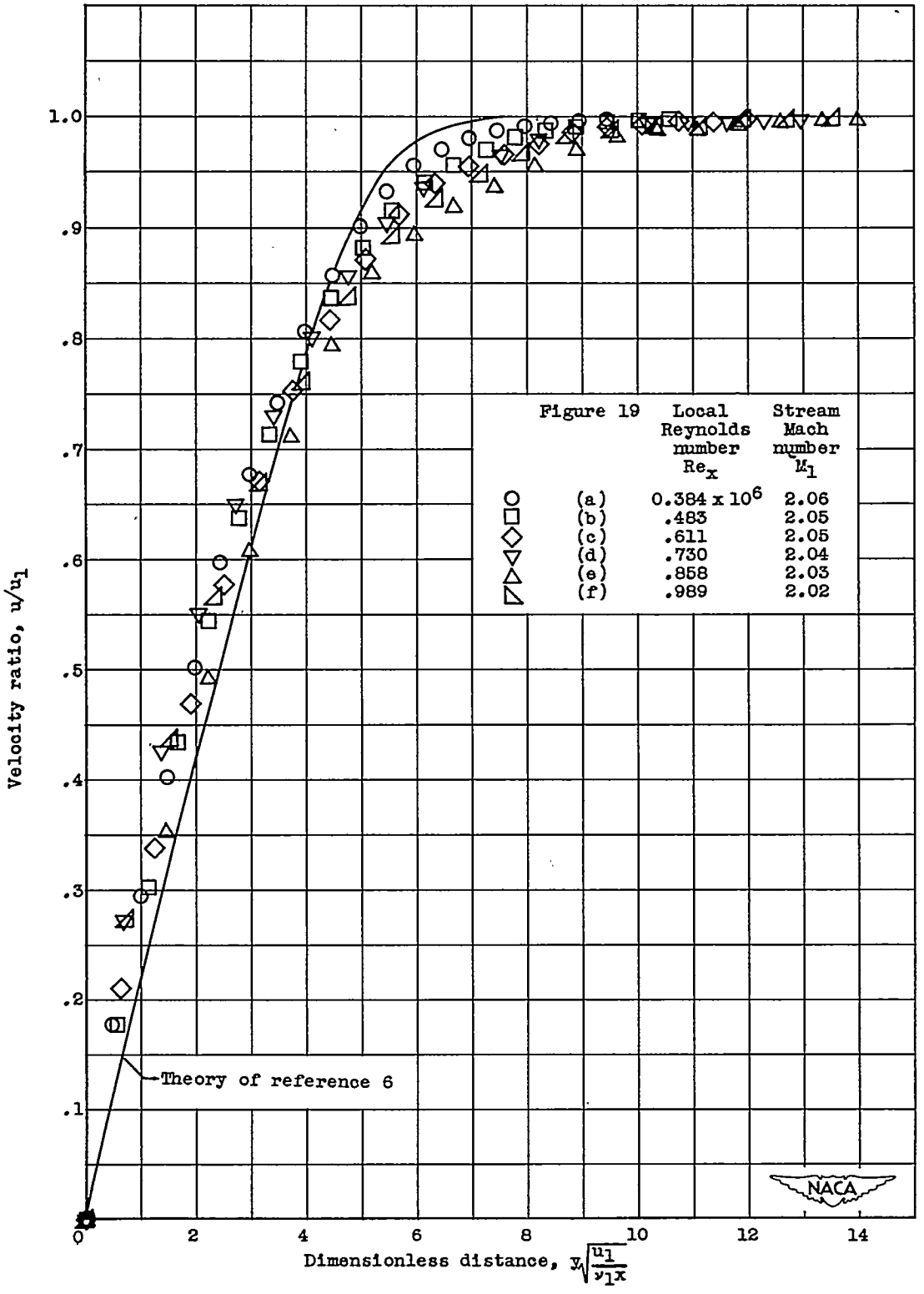

(a) Interference measurements.

Figure 22. - Velocity profiles from interference and total-pressure measurements.

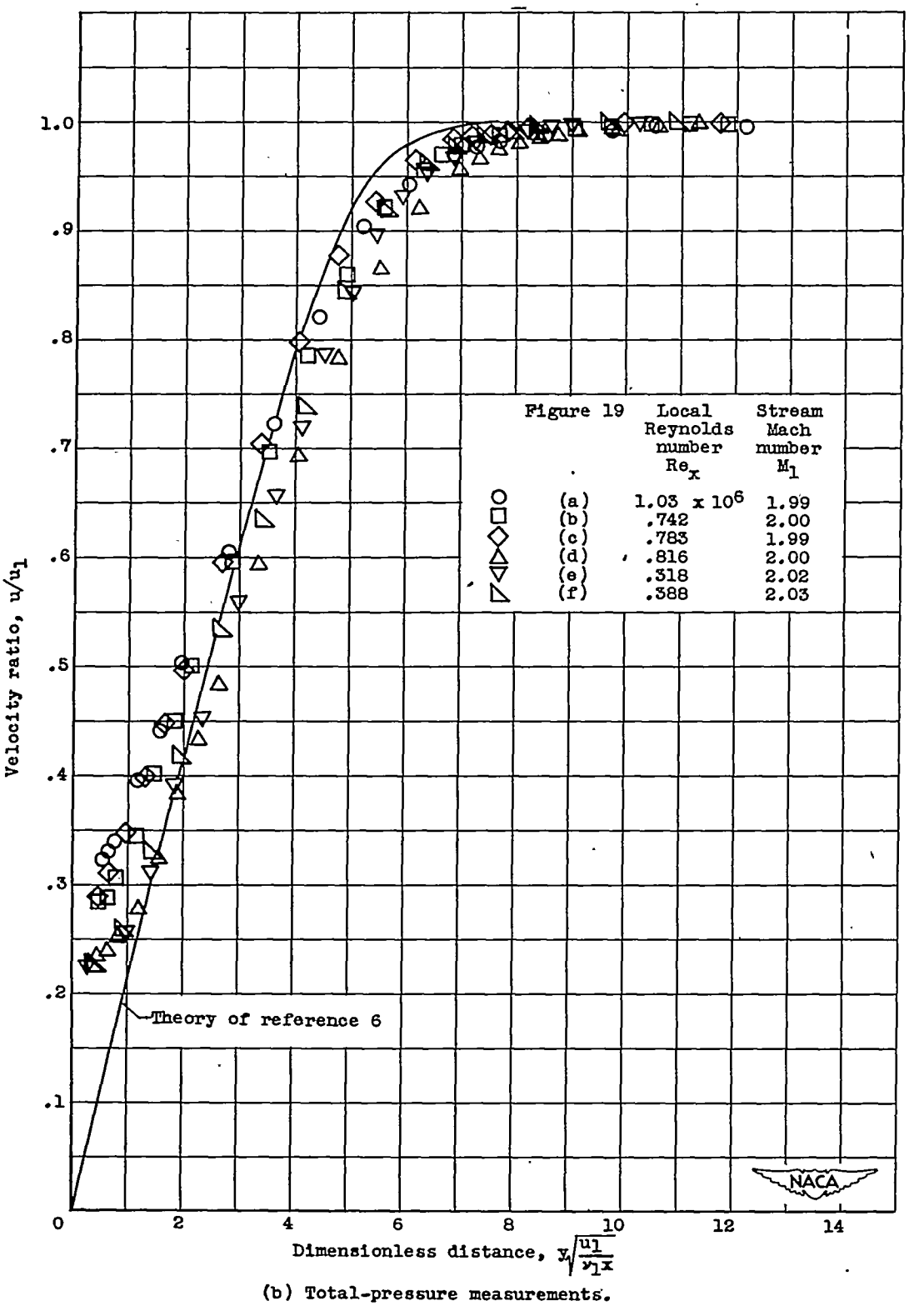

(b) Total-pressure measurements.

Figure 22. - Concluded. Velocity profiles from interference and total-pressure measurements.

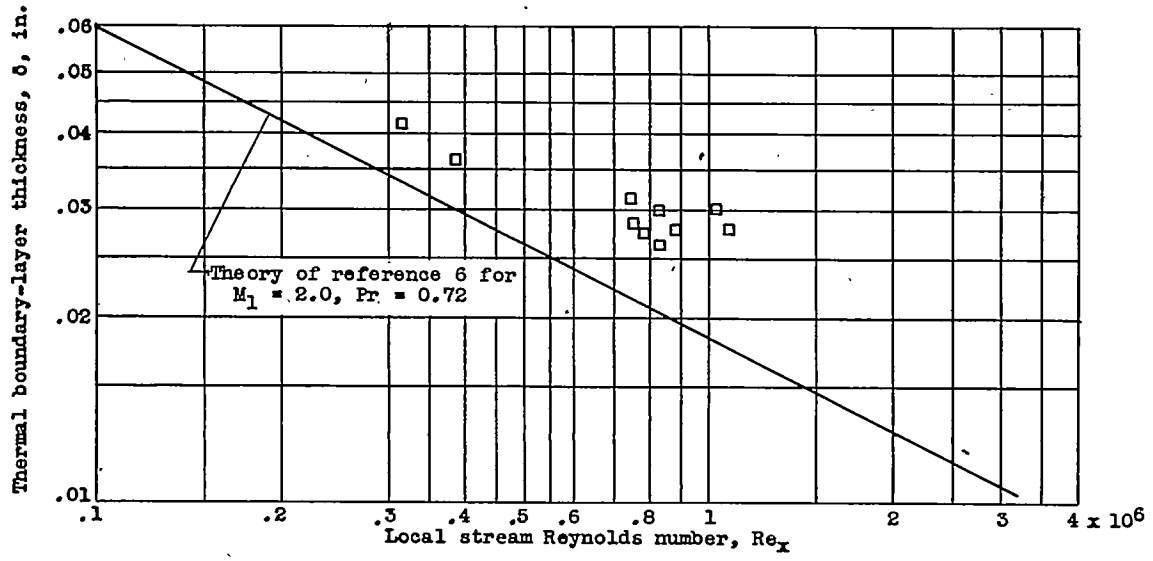

Figure 23. - Thermal boundary-layer thickness obtained from total-pressure measurements as function of local stream Reynolds number; x = $2\frac{1}{2}$ inches.

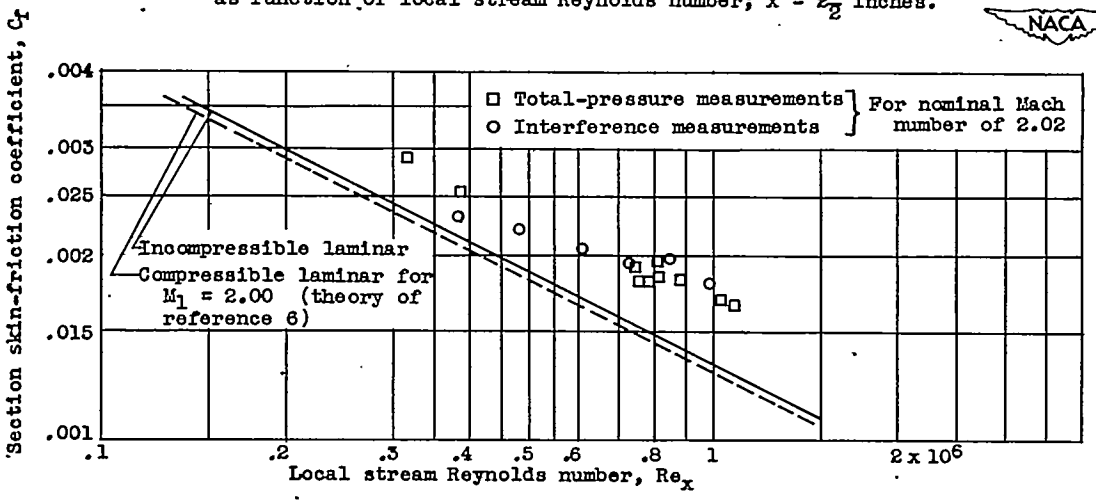

Figure 24. - Section skin-friction coefficient as function of local stream Reynolds number calculated from interference and total-pressure measurements; x = $2\frac{1}{2}$ inches.

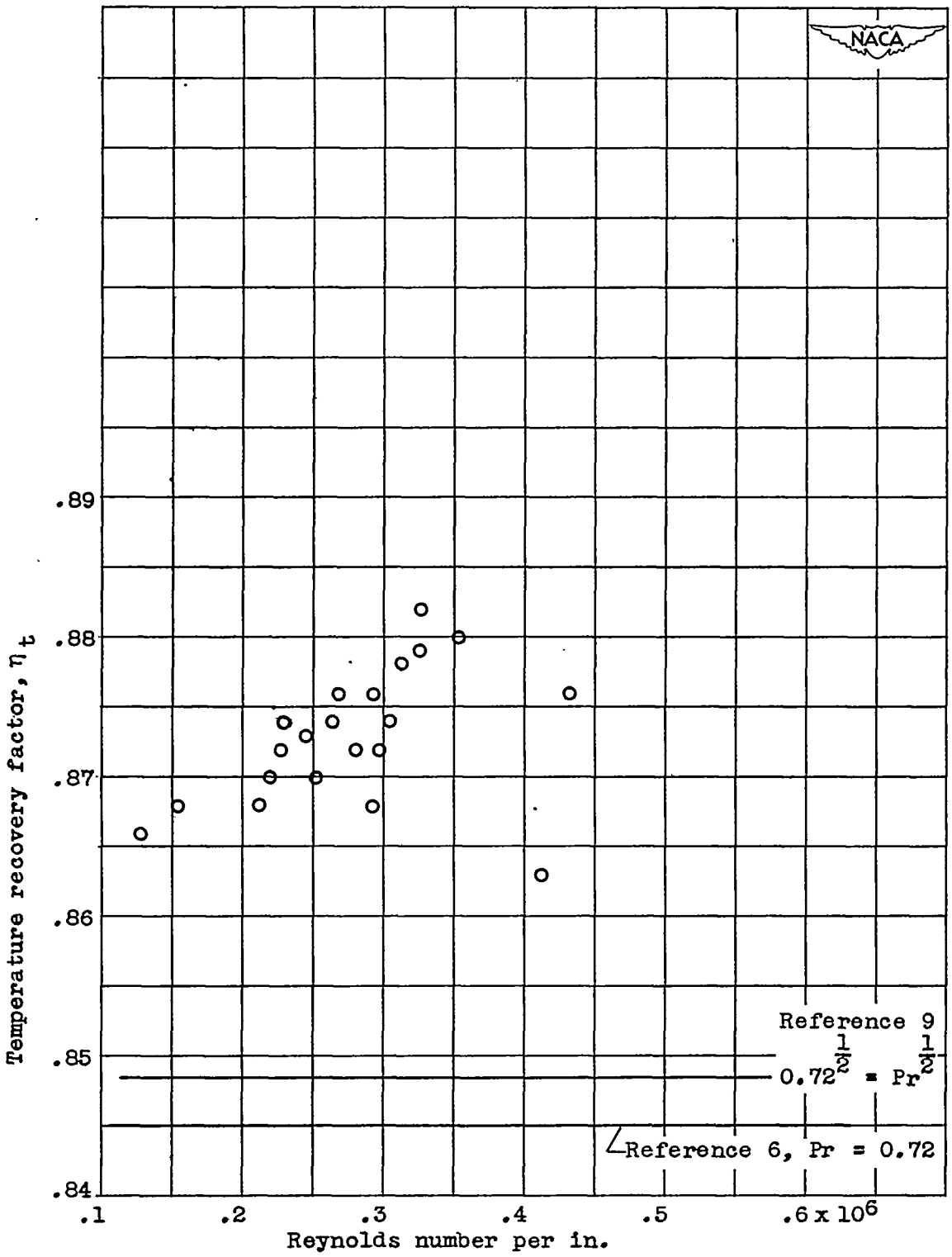

Figure 25. - Temperature recovery factor as function of Reynolds number in test section.

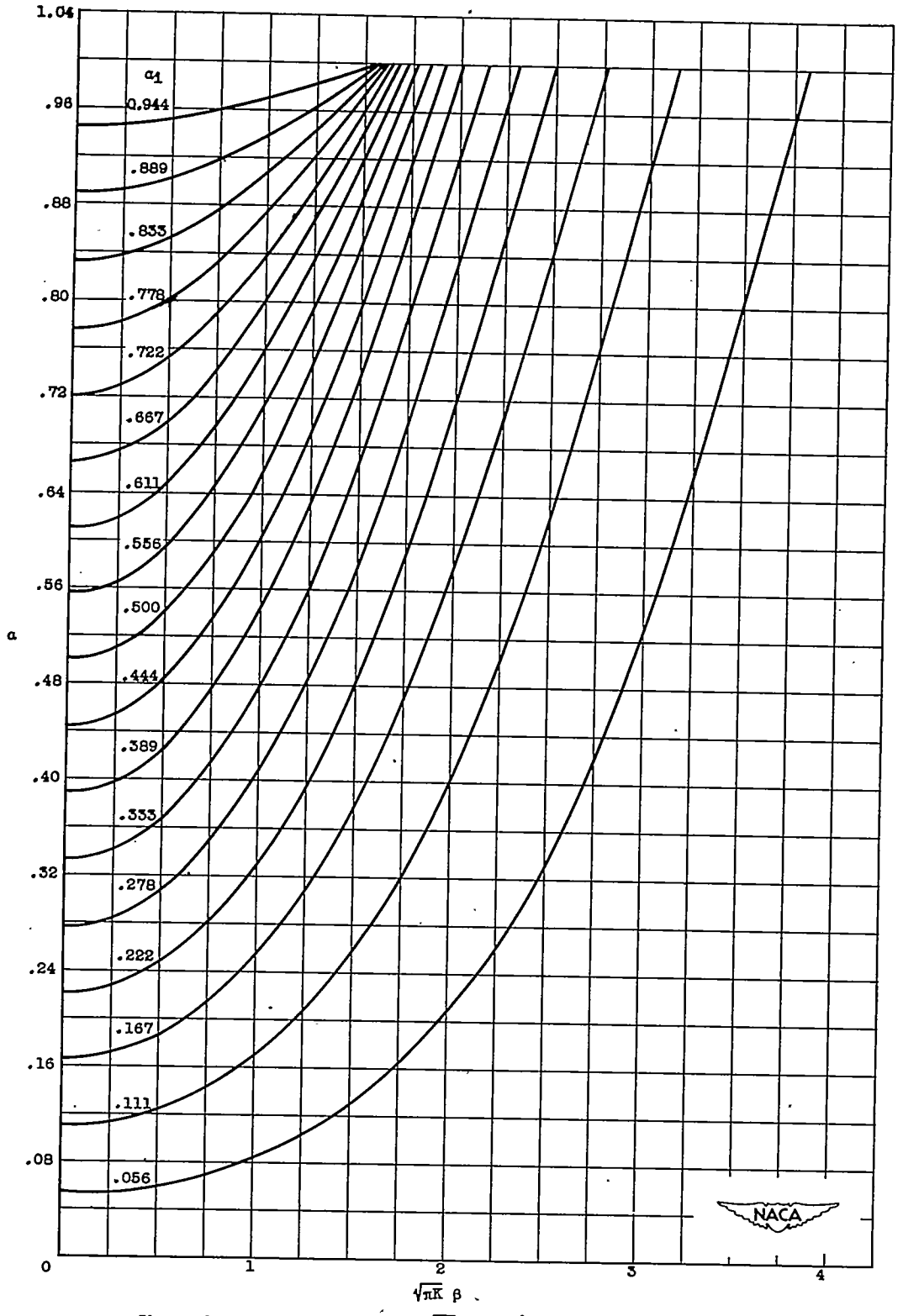

Figure 26. - a as function of $\sqrt{\pi K}\ \beta$ evaluated from equation (B7).

$$\sqrt{\pi K}\ \beta = \frac{\pi}{\sqrt{2}} \int_{a_1}^{a} \frac{da}{\sqrt{\cos \pi a_1 - \cos \pi a}}$$

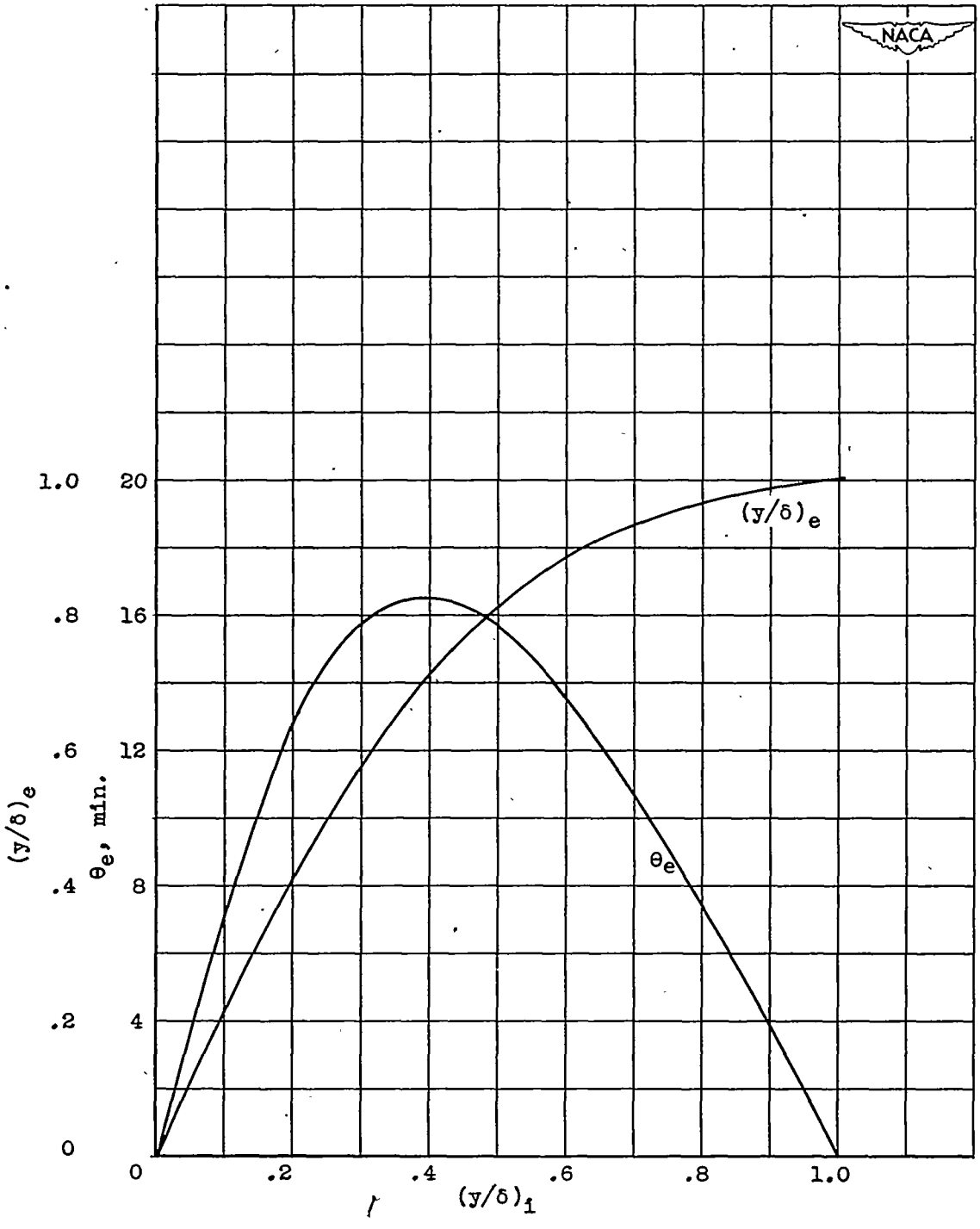

Figure 27. - Emergent height and angle of light as function of entrance height.

NACA-Langley - 6-8-50 - 1025